



Constitutive modeling of strain induced grain boundary migration via coupling crystal plasticity and phase-field methods



M. Jafari^a, M. Jamshidian^{a,*}, S. Ziaei-Rad^a, D. Raabe^b, F. Roters^b

^a Department of Mechanical Engineering, Isfahan University of Technology, Isfahan 84156-83111, Iran

^b Max-Planck-Institut für Eisenforschung, Max-Planck-Straße 1, 40237 Düsseldorf, Germany

ARTICLE INFO

Article history:

Received 14 June 2017

Received in revised form 13 August 2017

Accepted 25 August 2017

Available online 1 September 2017

Keywords:

Constitutive modeling

Strain induced boundary migration

Crystal plasticity

Phase field

Finite elements

ABSTRACT

We have developed a thermodynamically-consistent finite-deformation-based constitutive theory to describe strain induced grain boundary migration due to the heterogeneity of stored deformation energy in a plastically deformed polycrystalline cubic metal. Considering a representative volume element, a mesoscale continuum theory is developed based on the coupling between dislocation density-based crystal plasticity and phase field methods. Using the Taylor model-based homogenization method, a multiscale coupled finite-element and phase-field staggered time integration procedure is developed and implemented into the Abaqus/Standard finite element package via a user-defined material subroutine. The developed constitutive model is then used to perform numerical simulations of strain induced grain boundary migration in polycrystalline tantalum. The simulation results are shown to qualitatively and quantitatively agree with experimental results.

© 2017 Elsevier Ltd. All rights reserved.

1. Introduction

Polycrystalline microstructure of metallic materials can be tailored to specific engineering needs by optimizing the evolution of microstructure via grain boundary migration (Stojakovic et al., 2008; Ciulik and Taleff, 2009). Therefore, understanding the mechanisms and driving forces for grain boundary migration is necessary for producing metals with superior properties via controlling the microstructural characteristics such as crystallographic texture and grain size. During plastic deformation, most of the plastic work is converted into heat. However, a small portion of the plastic work is stored in dislocation structures, the so-called *stored deformation energy* (Anand et al., 2015). Plastic anisotropy of grains in a polycrystalline microstructure results in a stored energy difference across grain boundaries which in turn can provide a driving force sufficient for grain boundary migration in a number of processes (Humphreys and Hatherly, 2004; Raabe, 2014). Strain induced grain boundary migration (SIBM) is known as the migration of a pre-existing grain boundary segment driven by the stored energy difference across that grain boundary (Humphreys and Hatherly, 2004; Raabe, 2014). The region swept by a grain boundary via SIBM acquires a reduced dislocation content (Beck and Sperry, 1950). Therefore, consistent with the second law of thermodynamics, SIBM generally reduces the total stored deformation energy of a plastically deformed

* Corresponding author.

E-mail address: jamshidian@cc.iut.ac.ir (M. Jamshidian).

microstructure. *Static* SIBM refers to the case when microstructure evolution occurs subsequent to plastic deformation, while *Dynamic* SIBM refers to the case of simultaneous plastic deformation and microstructure evolution.

There is some experimental evidence for the occurrence of SIBM (Raabe et al., 1994). For instance, experiments on aluminum bicrystals showed that after plastic deformation and during annealing the cube texture $\{001\}\langle 100 \rangle$ intensifies rapidly in comparison with other texture components because of its low stored deformation energy (Theyssier and Driver, 1999; Kashiwara et al., 2011). By introducing an in-situ observation method for microstructural changes during hot deformation, Yogo et al. (2009) were able to detect the onset and measure the rate of SIBM for carbon steel. As an application, Stojakovic et al. (2008) utilized *Static* SIBM and developed a processing route to recover the desired fiber texture of iron-silicon electrical steel. They found that two steps of light rolling and subsequent annealing greatly restores the pre-existing desired fiber texture having a low stored deformation energy. Recently, Tallef and co-workers (Ciulik and Taleff, 2009; Taleff and Pedrazas, 2013; Noell and Taleff, 2015) utilized *dynamic* SIBM to produce large single crystals of molybdenum and tantalum from polycrystalline samples in the solid state.

Regarding the theoretical studies of SIBM, Battaile et al. (2007) developed a simulation method for the interplay between deformation and microstructure evolution by combining a two-dimensional sharp-interface front tracking model for grain boundary migration and a finite-element polycrystal plasticity model for deformation. Abrivard et al. (2012a, b) coupled the phase field and crystal plasticity approaches to simulate SIBM in aluminum bicrystalline and polycrystalline samples. They concluded that the final microstructure is composed of grains with the lowest stored energy values. The focus of their simulations was mostly on static SIBM and they only investigated *dynamic* SIBM for low strain values of about 1%. In a recent similar study, Zhao et al. (2017) used a combination of phase field and crystal plasticity models to simulate SIBM in bicrystalline samples and demonstrated that the heterogeneity of stored deformation energy provides a strong driving force for SIBM, especially at large strain values. Though providing some valuable insights, none of the aforementioned studies portray correspondence and similitude with the available experimental data on SIBM. Also, the previous models have mostly concentrated on the numerical coupling between crystal plasticity and phase field methods rather than on a theoretical coupling based on a thermodynamically-consistent methodology. In this methodology, grain boundary migration and plasticity effects are coupled within a consistent thermodynamical framework in which the derivation of the coupled constitutive theory is directed and restricted by the second law of thermodynamics.

Established upon the diffuse interface description of the grain boundary, the phase field modeling approach has emerged as a promising computational tool for the modeling of microstructure evolution in a wide range of applications involving complex morphological evolution (Chen, 2002; Kim et al., 2006; Moelans et al., 2008; Steinbach, 2009). The phase field method has been widely used for the modeling of recrystallization as a process involving plastic deformation and grain boundary migration (Takaki et al., 2014; Chen et al., 2015; Zhao et al., 2016; de Rancourt et al., 2016). Thamburaja and Jamshidian (2014) reformulated the phase field theory into a thermodynamically-consistent framework and derived constitutive relations for stressed grain growth in an elastically-deformed polycrystalline RVE. They also implemented their constitutive theory into the Abaqus/Standard finite element package using a multiscale Taylor model-based homogenization approach and a sequentially-coupled staggered numerical algorithm. They later demonstrated that such a constitutive model is able to qualitatively and quantitatively predict the evolution of microstructure and texture of polycrystalline thin films during post deposition annealing (Jamshidian and Rabczuk, 2014; Jamshidian et al., 2016). However, this model was limited to elastic deformation i.e. the grain boundary migration driving force arising from the stored energy in dislocation structures was neglected.

Combined with the phase field approach, the well-documented continuum theory of crystal plasticity (Anand, 2004; Gurtin et al., 2007; Chen et al., 2015; Shanthraj et al., 2015; Vondrous et al., 2015; Popova et al., 2015; Raabe and Becker, 2000; Roters et al., 2010) is commonly used to model the plastic deformation of a polycrystalline RVE as an aggregate of differently oriented individual crystals. Recently, Anand et al. (2015) developed a thermodynamically-consistent dislocation density-based gradient theory of single-crystal plasticity. They derived expressions for the fraction of plastic stress power that converts to heat and discussed the reduction of the dislocation density during annealing as a dissipative process.

The main objective of the present study is to develop a thermodynamically-consistent constitutive model for SIBM by utilizing the phase field and crystal plasticity approaches. Particularly, a finite deformation and dislocation density-based single crystal plasticity theory (Anand et al., 2015; Jafari et al., 2017) is used to augment the previously developed phase field theory of stressed grain growth (Thamburaja and Jamshidian, 2014) by including the extra driving force arising from the heterogeneity of the stored deformation energy. Using the multiscale Taylor model-based homogenization method (Taylor, 1938), a sequentially-coupled staggered time integration procedure is developed and implemented into the Abaqus/Standard finite element package via writing a user material subroutine UMAT. The constitutive model is then used to perform quantitative simulations of dynamic SIBM in polycrystalline tantalum. This paper ends with a discussion on the simulation results and the similarities with the experimental data available in the literature.

2. Mesoscale continuum theory

The constitutive model developed in this work is intended for the modeling of microstructure evolution due to grain boundary migration in a mesoscale domain of a representative volume element (RVE) representing a macroscale material point as shown in Fig. 1. Particularly, we develop a mesoscale continuum constitutive theory describing strain induced grain boundary migration mainly driven by the heterogeneity of the stored deformation energy across grain boundary. The

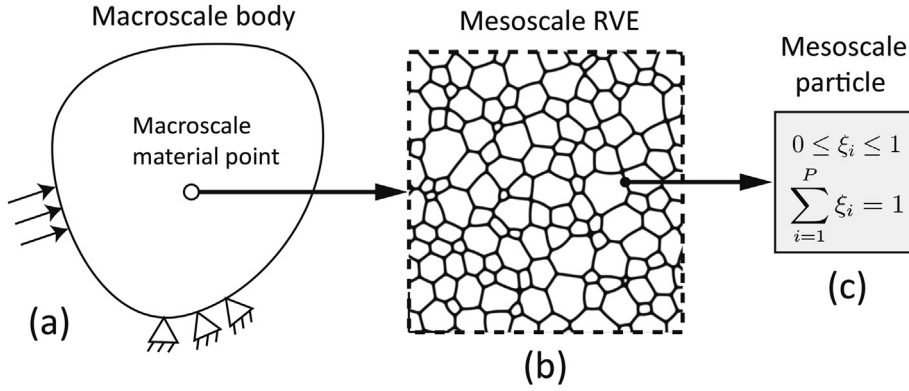


Fig. 1. (a) A macroscale continuum body under thermo-mechanical loading and a typical macroscale material point within. (b) The mesoscale representative volume element (RVE) attached to the macroscale material point and a typical mesoscale particle within. The RVE comprises P unique species/single crystal orientations. (c) Each mesoscale particle is composed of multiple species with the scalar variable ξ_i denoting the volume fraction of species i .

constitutive theory exploits the coupling between the dislocation density-based crystal viscoplasticity approach for describing the evolution of stored deformation energy and the phase field approach for describing the diffuse interface motion of grain boundaries. The constitutive theory is developed using the principle laws of thermodynamics and the theory of microforce balance (Fried and Gurtin, 1994; Gurtin, 2008). As suggested by Thamburaja and Jamshidian (2014), we develop the present constitutive framework under isothermal conditions and in the absence of heat fluxes/sources. Also, the mesoscale body/inertial forces and the effect of the body external surfaces on grain boundary motion will be neglected. Focusing on a mesoscale material particle within the RVE as shown in Fig. 1, all the mesoscale balance equations, constitutive equations and thermodynamic laws will be formulated in the reference configuration. Furthermore, we shall term each unique single-crystal orientation as a *species* where P represents the total number of unique species in the polycrystalline RVE. In other words, the term species is used for a structural non-conserved field variable of the Ginzburg Landau phase field formalism.

2.1. Governing variables

Let ∇ , Div and $\nabla\nabla$ denote the gradient, divergence and second gradient operators in the *reference* configuration, respectively. Considering a typical mesoscale particle in the RVE, the governing variables in the mesoscale constitutive model are: (a) the Helmholtz free energy per unit *reference* volume, ψ ; (b) the deformation gradient, \mathbf{F} with $J = \det \mathbf{F} > 0$; (c) the *velocity gradient*, $\mathbf{L} = \dot{\mathbf{F}}\mathbf{F}^{-1}$ where $\dot{\mathbf{F}}$ is the material time derivative of \mathbf{F} (d) the (absolute) temperature, $\theta > 0$; (e) the Cauchy stress \mathbf{T} , where $\mathbf{T} = \mathbf{T}^T$ by the balance of angular momentum; (f) the volume fraction of single-crystal orientation/species i at the mesoscale particle, ξ_i where $0 \leq \xi_i \leq 1$ with $i = 1, 2, \dots, P$, and $\sum_{i=1}^P \xi_i = 1$. A value of $\xi_i = 0$ means that species i is not present whereas a value of $\xi_i = 1$ means that the mesoscale particle fully consists of species i . A mesoscale particle which contains a mixture of two or more species represents a part of a *grain boundary* region; (g) the microstress vector \mathbf{h}_i (measured per unit area in the *reference* configuration) which acts in response to changes in the volume fraction of species i where $i = 1, 2, \dots, P$; and finally (h) the density of dislocations associated with slip system α of species i , ρ_i^α with $\alpha = 1, \dots, N$ and $i = 1, \dots, P$, where N is the number of slip systems.

For convenience, we set the vector $\mathbf{m}_i = \nabla \xi_i$ for $i = 1, 2, \dots, P$, and list the volume fraction of species and its material gradient as $\xi = (\xi_1, \xi_2, \dots, \xi_P)$ and $\mathbf{m} = (\mathbf{m}_1, \mathbf{m}_2, \dots, \mathbf{m}_P)$, respectively. We also represent $\vec{\rho}_i = (\rho_i^1, \rho_i^2, \dots, \rho_i^N)$ as the list containing the dislocation density of all slip systems in species i with $i = 1, \dots, P$; and finally $\vec{\rho} = (\vec{\rho}_1, \vec{\rho}_2, \dots, \vec{\rho}_P)$ as the list containing the dislocation density of all slip systems of all species.

2.2. Second law of thermodynamics

Under isothermal condition i.e. $\dot{\theta} = 0$, the local form of the second law of thermodynamics in the *reference* configuration is given by (Thamburaja and Jamshidian, 2014)

$$\Pi^s + \sum_{i=1}^P \left\{ (\text{Div } \mathbf{h}_i) \dot{\xi}_i + \mathbf{h}_i \cdot \mathbf{m}_i \right\} \geq \dot{\psi}, \quad (1)$$

with the mesoscale *stress power* given by

$$\Pi^S = \mathbf{J} \mathbf{T} : \mathbf{L}. \quad (2)$$

Due to the mixture of multiple species, the mesoscale stress power is supposed to be given by the following smooth-interpolation (Moelans, 2011; Thamburaja and Jamshidian, 2014) over the individual stress power of the species constituting a mesoscale particle as

$$\Pi^S = \frac{\sum_{i=1}^P g(\xi_i) \Pi_i^S}{\sum_{i=1}^P g(\xi_i)}, \quad (3)$$

with the smooth interpolation scalar function $g(\xi_i) = \xi_i^2(3 - 2\xi_i)$ and the stress power of each species i for $i = 1, 2, \dots, P$ given by

$$\Pi_i^S = \mathbf{J}_i \mathbf{T}_i : \mathbf{L}_i \quad \text{with} \quad \mathbf{J}_i = \det \mathbf{F}_i, \quad (4)$$

where \mathbf{F}_i , \mathbf{T}_i and \mathbf{L}_i represent the deformation gradient tensor, the velocity gradient tensor and the Cauchy stress tensor of species i , respectively. In the present study, we assume that for all time the deformation gradient of each individual species constituting a mesoscale particle is the same as the deformation gradient applied to the mesoscale particle; in other words

$$\mathbf{F} = \mathbf{F}_i \Rightarrow \mathbf{L} = \mathbf{L}_i, \quad \mathbf{J} = \mathbf{J}_i \quad \text{and} \quad \mathbf{C} = \mathbf{C}_i, \quad (5)$$

where $\mathbf{C} = \mathbf{F}^T \mathbf{F}$ and $\mathbf{C}_i = \mathbf{F}_i^T \mathbf{F}_i$ represent the mesoscale right Cauchy-Green deformation tensor and right Cauchy-Green deformation tensor for the species i , respectively.

2.3. Microkinematical hypotheses

Following the works of Anand (2004) and Lele and Anand (2009), for each species i the total deformation gradient is represented by the multiplicative decomposition

$$\mathbf{F}_i = \mathbf{F}_i^e \mathbf{F}_i^p, \quad (6)$$

where \mathbf{F}_i^p represents the *plastic* part of \mathbf{F} due to the motion of dislocations and \mathbf{F}_i^e being the *elastic* part of \mathbf{F} due to the elastic mechanisms of stretching and rotation of the lattice. We also define the velocity gradient tensor of each species i as

$$\mathbf{L}_i = \dot{\mathbf{F}}_i \mathbf{F}_i^{-1}, \quad (7)$$

for $i = 1, 2, \dots, P$. Combining Eqs. (6) and (7) leads to the additive decomposition of the velocity gradient of species i as

$$\mathbf{L}_i = \mathbf{L}_i^e + \mathbf{F}_i^e \mathbf{L}_i^p \mathbf{F}_i^{e-1}, \quad (8)$$

where $\mathbf{L}_i^e = \dot{\mathbf{F}}_i^e \mathbf{F}_i^{e-1}$ and $\mathbf{L}_i^p = \dot{\mathbf{F}}_i^p \mathbf{F}_i^{p-1}$ are the elastic and plastic *distortion rates* of species i , respectively. The tensor \mathbf{L}_i^p is related to dislocation motion as the plastic deformation occurs by the motion of dislocations. It is assumed that the dislocation motion occurs on prescribed slip systems $\alpha = 1, 2, \dots, N$ in the lattice where each slip system is defined by a *slip plane normal* $\mathbf{m}_{i,0}^\alpha$ and a *slip direction* $\mathbf{s}_{i,0}^\alpha$ for species $i = 1, 2, \dots, P$. Denoting *microshear-rates* on slip system α of species i by $\dot{\gamma}_i^\alpha$, with $\alpha = 1, 2, \dots, N$ and $i = 1, 2, \dots, P$, the plastic *distortion rate* tensor for species i is expressed by (Anand, 2004)

$$\mathbf{L}_i^p = \sum_{\alpha=1}^N \dot{\gamma}_i^\alpha \mathbf{S}_{i,0}^\alpha, \quad (9)$$

where $\mathbf{S}_{i,0}^\alpha = \mathbf{s}_{i,0}^\alpha \otimes \mathbf{m}_{i,0}^\alpha$ is referred to as the *Schmid tensor* corresponding to slip system α of species i .

We define the elastic strain tensor of each species i as (Anand, 2004)

$$\mathbf{E}_i^e = 1/2 (\mathbf{F}_i^{eT} \mathbf{F}_i^e - \mathbf{I}) \quad (10)$$

and denote $\mathbf{E}^e = (\mathbf{E}_1^e, \mathbf{E}_2^e, \dots, \mathbf{E}_P^e)$ as the list containing the elastic strain tensor of all species. Defining the symmetric *true lattice stress* (Gurtin, 2000) of species i as

$$\mathbf{T}_i^e = \mathbf{J}_i \mathbf{F}_i^{e-1} \mathbf{T}_i \mathbf{F}_i^{e-T}, \quad (11)$$

and substituting Eq. (8) in Eq. (4) results in the decomposition of the stress power term of species i into the elastic and plastic parts as follow

$$\Pi_i^s = \mathbf{T}_i^e : \dot{\mathbf{E}}_i^e + \mathbf{C}_i^e \mathbf{T}_i^e : \mathbf{L}_i^p, \quad (12)$$

with $\dot{\mathbf{E}}_i^e$ being the material time derivative of the elastic strain tensor of species i and $\mathbf{C}_i^e = \mathbf{F}_i^{e\top} \mathbf{F}_i^e$ the elastic right Cauchy-Green deformation tensor of species i . Also, substituting Eq. (9) in the last term on the right hand side of Eq. (12) leads to the plastic stress power of species i as

$$\mathbf{C}_i^e \mathbf{T}_i^e : \mathbf{L}_i^p = \sum_{\alpha=1}^N \tau_i^\alpha \dot{\gamma}_i^\alpha, \quad (13)$$

where $\tau_i^\alpha = \mathbf{C}_i^e \mathbf{T}_i^e : \mathbf{S}_{i,0}^\alpha$ is the *resolved shear stress* on slip system α of species i with $\alpha = 1, 2, \dots, N$ and $i = 1, 2, \dots, P$. Finally, substituting Eq. (13) in Eq. (12) and the result in Eq. (3) and the result of them in Eq. (1) results in

$$\frac{\sum_{i=1}^P g(\xi_i) \left(\mathbf{T}_i^e : \dot{\mathbf{E}}_i^e + \sum_{\alpha=1}^N \tau_i^\alpha \dot{\gamma}_i^\alpha \right)}{\sum_{i=1}^P g(\xi_i)} + \sum_{i=1}^P \left\{ (\text{Div } \mathbf{h}_i) \dot{\xi}_i + \mathbf{h}_i \cdot \dot{\mathbf{m}}_i \right\} \geq \dot{\psi}. \quad (14)$$

2.4. Free energy

Using the principle of material frame-indifference (Anand, 2004; Thamburaja and Jamshidian, 2014) and the works of Fried and Gurtin (1994); Steinbach and Pezzolla (1999); Tonks and Millett (2011); Gurtin et al. (2007) and Anand et al. (2015), the Helmholtz free energy per unit *reference* volume, $\psi = \hat{\psi}(\vec{p}, \mathbf{E}^e, \theta, \xi, \mathbf{m})$ is taken to be

$$\psi = \left(\frac{\sum_{i=1}^P g(\xi_i) \psi_i}{\sum_{i=1}^P g(\xi_i)} \right) + \psi^m. \quad (15)$$

The first term on the right-hand side of Eq. (15) represents the *composite* free energy due to the mixture of multiple species where $\psi_i = \hat{\psi}_i(\vec{p}_i, \mathbf{E}_i^e, \theta)$ indicates the intrinsic free energy of species i with the smooth interpolation scalar function $g(\xi_i) = \xi_i^2(3 - 2\xi_i)$ (Bhattacharyya et al., 2011). With integers $i = 1, 2, \dots, P$, the microstructural free energy, ψ^m is given by (Steinbach and Pezzolla, 1999; Thamburaja and Jamshidian, 2014)

$$\psi^m = (1/2) \sum_{i=1}^P \sum_{r \neq i}^P \omega_{ir}^\xi \xi_i \xi_r - (1/4) \sum_{i=1}^P \sum_{r \neq i}^P \varepsilon_{ir}^\xi \mathbf{C}^{-1} : (\mathbf{m}_i \otimes \mathbf{m}_r)$$

where $\omega_{ir}^\xi = \omega_{ri}^\xi$ (units of energy per unit volume) define the constant potential energy barriers between species i and r in order to prevent spontaneous conversions between these two species, and $\varepsilon_{ir}^\xi = \varepsilon_{ri}^\xi$ (units of energy per unit length) represent the constant gradient energy coefficients which control the grain boundary thickness between species i and r . The dependency of the microstructural free energy on deformation tensor \mathbf{C} is included to account for the effect of distortion on grain boundary migration (Jamshidian et al., 2014).

The intrinsic free energy of each species i , ψ_i is taken to be

$$\psi_i = \psi_i^e + \psi_i^\theta + \psi_i^p,$$

where the *thermo-elastic* free energy $\psi_i^e = \hat{\psi}_i^e(\mathbf{E}_i^e, \theta)$ and the *purely thermal* free energy $\psi_i^\theta = \hat{\psi}_i^\theta(\theta)$ of each species i are (Bloomfield et al., 2008; Tonks et al., 2010; Tonks and Millett, 2011)

$$\psi_i^e = (1/2) [\mathbf{E}_i^e - \alpha_{th} (\theta - \theta_0) \mathbf{I}] : \mathcal{E}_i [\mathbf{E}_i^e - \alpha_{th} (\theta - \theta_0) \mathbf{I}],$$

and

$$\psi_i^\theta = c_{th} [(\theta - \theta_0) - \theta \ln(\theta/\theta_0)],$$

respectively. With θ_0 being the reference temperature, the material constants \mathcal{E}_i , α_{th} and c_{th} represent the symmetric fourth-order elastic moduli tensor for species i , the thermal expansion coefficient and the specific heat, respectively.

Following Anand et al. (2015) and Abrivard et al. (2012a), the defect/plastic free energy $\psi_i^p = \hat{\psi}_i^p(\vec{p}_i, \theta)$, for species i is taken to be

$$\psi_i^p = a \mu b^2 \sum_{\alpha=1}^N \rho_i^\alpha, \quad (16)$$

where a is a constant approximately equal to 0.5, μ is the shear modulus, and b is the magnitude of the Burgers vector.

2.5. Evolution of dislocation density

Following Anand et al. (2015) and Abrivard et al. (2012a), the evolution of the dislocation density associated with slip system α of species i due to the mechanisms of dislocation generation, dislocation annihilation and SIBM-induced dislocation reduction is assumed to obey the following phenomenological kinetic relation

$$\dot{\rho}_i^\alpha = K_1 \sqrt{\rho_i^\alpha} |\dot{\gamma}_i^\alpha| - K_2 \rho_i^\alpha - \rho_i^\alpha C_d \dot{\xi}_i \text{step}(\dot{\xi}_i) \quad \text{with} \quad \rho_i^\alpha|_{t=0} = \rho_{i,0}^\alpha, \quad (17)$$

with $\alpha = 1, 2, \dots, N$ and $i = 1, 2, \dots, P$, $\rho_{i,0}^\alpha$ being the corresponding initial dislocation density and the step function defined by

$$\text{step}(\dot{\xi}_i) = \begin{cases} 1 & \text{if } \dot{\xi}_i > 0, \\ 0 & \text{if } \dot{\xi}_i \leq 0. \end{cases}$$

The first term on the right hand side of Eq. (17) describes dislocation generation due to plastic flow/microshear with $K_1 \geq 0$ being the *dislocation-accumulation* modulus; while the second term on the right hand side of Eq. (17) represents dislocation annihilation due to thermal annealing with $K_2 \geq 0$ denoting the *recovery rate* modulus. There exists experimental evidence that when a grain boundary moves through a defected material, the dislocation density in the region swept by the boundary decreases to a large extent (Humphreys and Hatherly, 2004; Battaile et al., 2007; Abrivard et al., 2012a; Raabe, 2014). Therefore, the third term on the right hand side of Eq. (17) is included to characterize dislocation reduction behind a moving grain boundary. This term introduces an explicit dependence for the decrease rate of the dislocation density on the evolution of the phase field variable via the proportionality constant $C_d \geq 0$. The rate of dislocation reduction increases with increasing values of C_d . Sufficiently large values of C_d resets the dislocation density to its initial state, identified by $\rho_{i,0}^\alpha$. Also, in this term the aim of the switching multiplier $\text{step}(\dot{\xi}_i)$ is to localize the SIBM-induced dislocation reduction in the close rear vicinity of the migrating grain boundary, while leaving the dislocation density ahead of the moving grain boundary intact.

2.6. Dissipation inequality

Under isothermal condition i.e. $\dot{\theta} = 0$, the material time derivative of Eq. (15) is

$$\dot{\psi} = \frac{\sum_{i=1}^P \left(g(\xi_i) \frac{\partial \psi_i}{\partial \mathbf{E}_i^e} : \dot{\mathbf{E}}_i^e \right)}{\sum_{i=1}^P g(\xi_i)} + \sum_{i=1}^P \left(\frac{\partial \psi}{\partial \mathbf{m}_i} \cdot \dot{\mathbf{m}}_i + \frac{\partial \psi}{\partial \xi_i} \dot{\xi}_i \right) + \frac{\sum_{i=1}^P \sum_{\alpha=1}^N g(\xi_i) \mathcal{F}_i^\alpha \dot{\rho}_i^\alpha}{\sum_{i=1}^P g(\xi_i)}, \quad (18)$$

where the *energetic defect forces* are defined as

$$\mathcal{F}_i^\alpha(\vec{\rho}_i, \theta) = \frac{\partial \psi_i}{\partial \rho_i^\alpha}. \quad (19)$$

Substituting Eqs. (15) and (16) in Eq. (19) results in

$$\mathcal{F}_i^\alpha = a \mu b^2 \geq 0. \quad (20)$$

Using Eqs. (17) and (20), we have

$$\mathcal{F}_i^\alpha \dot{\rho}_i^\alpha = \tau_{i,en}^\alpha \dot{\gamma}_i^\alpha - \mathcal{F}_i^\alpha K_2 \rho_i^\alpha - \mathcal{F}_i^\alpha \rho_i^\alpha C_d \dot{\xi}_i \text{step}(\dot{\xi}_i), \quad (21)$$

where the *energetic nonrecoverable generalized stress* $\tau_{i,en}^\alpha$ for slip system α of species i is defined by the constitutive relation

$$\tau_{i,en}^\alpha = \mathcal{F}_i^\alpha K_1 \sqrt{\rho_i^\alpha} \frac{\dot{\gamma}_i^\alpha}{|\dot{\gamma}_i^\alpha|}, \quad (22)$$

with $\alpha = 1, 2, \dots, N$ and $i = 1, 2, \dots, P$. Substituting Eq. (21) in Eq. (18) results in

$$\begin{aligned} \dot{\psi} = & \frac{\sum_{i=1}^P \left(g(\xi_i) \frac{\partial \psi_i}{\partial \mathbf{E}_i^e} : \dot{\mathbf{E}}_i^e \right)}{\sum_{i=1}^P g(\xi_i)} + \sum_{i=1}^P \left(\frac{\partial \psi}{\partial \mathbf{m}_i} \cdot \dot{\mathbf{m}}_i + \frac{\partial \psi}{\partial \xi_i} \dot{\xi}_i \right) + \frac{\sum_{i=1}^P \sum_{\alpha=1}^N g(\xi_i) \tau_{i,en}^\alpha \dot{\gamma}_i^\alpha}{\sum_{i=1}^P g(\xi_i)} \\ & - \frac{\sum_{i=1}^P \sum_{\alpha=1}^N g(\xi_i) \mathcal{F}_i^\alpha K_2 \rho_i^\alpha}{\sum_{i=1}^P g(\xi_i)} - \frac{\sum_{i=1}^P \sum_{\alpha=1}^N g(\xi_i) \mathcal{F}_i^\alpha \rho_i^\alpha C_d \dot{\xi}_i \text{step}(\dot{\xi}_i)}{\sum_{i=1}^P g(\xi_i)}. \end{aligned} \quad (23)$$

We then substitute Eq. (23) into inequality (14) to obtain

$$\begin{aligned} & \frac{1}{\sum_{i=1}^P g(\xi_i)} \sum_{i=1}^P g(\xi_i) \left(\mathbf{T}_i^e - \frac{\partial \psi_i}{\partial \mathbf{E}_i^e} \right) : \dot{\mathbf{E}}_i^e + \sum_{i=1}^P \left(\mathbf{h}_i - \frac{\partial \psi}{\partial \mathbf{m}_i} \right) \cdot \dot{\mathbf{m}}_i + \frac{\sum_{i=1}^P \sum_{\alpha=1}^N g(\xi_i) \tau_{i,dis}^\alpha \dot{\gamma}_i^\alpha}{\sum_{i=1}^P g(\xi_i)} + \\ & \sum_{i=1}^P \left(\text{Div } \mathbf{h}_i - \frac{\partial \psi}{\partial \xi_i} \right) \dot{\xi}_i + \frac{\sum_{i=1}^P \sum_{\alpha=1}^N g(\xi_i) \mathcal{F}_i^\alpha K_2 \rho_i^\alpha}{\sum_{i=1}^P g(\xi_i)} + \frac{\sum_{i=1}^P \sum_{\alpha=1}^N g(\xi_i) \mathcal{F}_i^\alpha \rho_i^\alpha C_d \dot{\xi}_i \text{step}(\dot{\xi}_i)}{\sum_{i=1}^P g(\xi_i)} \geq 0, \end{aligned} \quad (24)$$

where the *dissipative microscopic stress* $\tau_{i,dis}^\alpha$ for slip system α of species i defined as

$$\tau_{i,dis}^\alpha = \tau_i^\alpha - \tau_{i,en}^\alpha, \quad (25)$$

with $\alpha = 1, 2, \dots, N$ and $i = 1, 2, \dots, P$.

2.7. Constitutive equations for stress and micro-traction

Using standard thermodynamics arguments (Fried and Gurtin, 1994; Anand et al., 2015) in inequality (24) and assuming that the stresses $\tau_{i,dis}^\alpha$ are independent of $\dot{\mathbf{E}}_i^e$ for each species i , we get the constitutive equations for the elastic stress and the micro-traction vectors of species i as

$$\mathbf{T}_i^e = \frac{\partial \psi_i}{\partial \mathbf{E}_i^e} = \mathcal{C}_i [\mathbf{E}_i^e - \alpha_{th}(\theta - \theta_0) \mathbf{I}] \quad \text{with } i = 1, 2, \dots, P, \quad (26)$$

and

$$\mathbf{h}_i = \frac{\partial \psi}{\partial \mathbf{m}_i} = \sum_{r \neq i}^P -\frac{\varepsilon_{ir}^\xi}{2} \mathbf{C}^{-1} \mathbf{m}_r \quad \text{with } i = 1, 2, \dots, P, \quad (27)$$

respectively. Combining Eqs. (2) to (5), (11) and (26) gives the mesoscale Cauchy stress as

$$\mathbf{T} = \frac{1}{J} \frac{\sum_{i=1}^P g(\xi_i) \mathbf{F}_i^e \mathcal{C}_i [\mathbf{E}_i^e - \alpha_{th}(\theta - \theta_0) \mathbf{I}] \mathbf{F}_i^{eT}}{\sum_{i=1}^P g(\xi_i)}. \quad (28)$$

Substituting Eqs. (26) and (27) back into inequality (24), results in the *reduced* dissipation inequality as

$$\begin{aligned} & \frac{\sum_{i=1}^P \sum_{\alpha=1}^N g(\xi_i) \tau_{i,dis}^\alpha \dot{\gamma}_i^\alpha}{\sum_{i=1}^P g(\xi_i)} + \sum_{i=1}^P \left(\text{Div } \mathbf{h}_i - \frac{\partial \psi}{\partial \xi_i} \right) \dot{\xi}_i + \frac{\sum_{i=1}^P \sum_{\alpha=1}^N g(\xi_i) \mathcal{F}_i^\alpha K_2 \rho_i^\alpha}{\sum_{i=1}^P g(\xi_i)} \\ & + \frac{\sum_{i=1}^P \sum_{\alpha=1}^N g(\xi_i) \mathcal{F}_i^\alpha \rho_i^\alpha C_d \text{step}(\dot{\xi}_i) \dot{\xi}_i}{\sum_{i=1}^P g(\xi_i)} \geq 0. \end{aligned} \quad (29)$$

Following our previous assumptions $g(\xi_i) \geq 0$, $K_2 \geq 0$, $\mathcal{F}_i^\alpha \geq 0$ and $C_d \geq 0$, we have

$$g(\xi_i) \mathcal{F}_i^\alpha K_2 \rho_i^\alpha \geq 0 \Rightarrow \sum_{i=1}^P \sum_{\alpha=1}^N g(\xi_i) \mathcal{F}_i^\alpha K_2 \rho_i^\alpha \geq 0, \quad (30)$$

which represents the dissipation associated with recovery and

$$g(\xi_i) \mathcal{F}_i^\alpha \rho_i^\alpha C_d \text{step}\left(\frac{\dot{\xi}_i}{\xi_i}\right) \dot{\xi}_i \geq 0 \Rightarrow \sum_{i=1}^P \sum_{\alpha=1}^N g(\xi_i) \mathcal{F}_i^\alpha \rho_i^\alpha C_d \text{step}\left(\frac{\dot{\xi}_i}{\xi_i}\right) \dot{\xi}_i \geq 0, \quad (31)$$

which represents the dissipation due to SIBM-induced dislocation reduction. Use of Eqs. (30) and (31), reduces Eq. (29) to

$$\frac{\sum_{i=1}^P \sum_{\alpha=1}^N g(\xi_i) \tau_{i,dis}^\alpha \dot{\gamma}_i^\alpha}{\sum_{i=1}^P g(\xi_i)} + \sum_{i=1}^P \left(\text{Div } \mathbf{h}_i - \frac{\partial \psi}{\partial \xi_i} \right) \dot{\xi}_i \geq 0. \quad (32)$$

To satisfy inequality (32) we assume that the total dissipation due to microshear and the total dissipation arising from grain boundary migration are non-negative i.e.

$$\frac{\sum_{i=1}^P \sum_{\alpha=1}^N g(\xi_i) \tau_{i,dis}^\alpha \dot{\gamma}_i^\alpha}{\sum_{i=1}^P g(\xi_i)} \geq 0 \quad \text{and} \quad \sum_{i=1}^P \left(\text{Div } \mathbf{h}_i - \frac{\partial \psi}{\partial \xi_i} \right) \dot{\xi}_i \geq 0, \quad (33)$$

respectively. Overall, the total dissipation comprises four distinct types; the two former identified by Eqs. (30)₂ and (31)₂ are *naturally* non negative, while the two latter identified by Eqs. (33)₁ and (33)₂ are used to drive the respective kinetic relations.

2.8. Viscoplastic flow rule

To satisfy inequality (33)₁, we assume that the dissipation due to microshear on each individual slip system is strictly non-negative, and that each dissipation is also *strongly* dissipative i.e.

$$\tau_{i,dis}^\alpha \dot{\gamma}_i^\alpha > 0 \quad \text{for} \quad \dot{\gamma} \neq 0. \quad (34)$$

To satisfy (34), we follow the works of Anand (2004) and Gurtin et al. (2007) and use the following form of the viscoplastic flow rule for microshear on slip system α of species i as

$$\tau_{i,dis}^\alpha = S_i^\alpha R(|\dot{\gamma}_i^\alpha|) \frac{\dot{\gamma}_i^\alpha}{|\dot{\gamma}_i^\alpha|} \quad \text{with} \quad R(|\dot{\gamma}_i^\alpha|) = \left(\frac{|\dot{\gamma}_i^\alpha|}{\dot{\gamma}_0} \right)^m, \quad (35)$$

where $\dot{\gamma}_0 > 0$ and $m > 0$ are a constant reference strain-rate and the constant-rate sensitivity parameter, respectively. The *slip resistance* on slip system α of species i , $S_i^\alpha > 0$ with $\alpha = 1, 2, \dots, N$ and $i = 1, 2, \dots, P$ is a strength-like internal state variable which is governed by the following hardening equation¹ (Franciosi and Zaoui, 1982; Lee et al., 2010)

$$S_i^\alpha = \mu b \sqrt{\sum_{\beta} h^{\alpha\beta} \rho_i^\beta}, \quad (36)$$

where $h^{\alpha\beta}$ is the hardening matrix with $\alpha = 1, 2, \dots, N$ and $\beta = 1, 2, \dots, N$. Finally, substituting Eqs. (35) and (22) into Eq. (25) and rearranging results in the microshear rate on slip system α of species i as

$$\dot{\gamma}_i^\alpha = \dot{\gamma}_0^\alpha \left(\frac{|\tau_i^\alpha| - \mathcal{F}_i^\alpha K_1 \sqrt{\rho_i^\alpha}}{S_i^\alpha} \right)^{1/m} \text{sign}(\tau_i^\alpha), \quad (37)$$

where the sign function defined by

$$\text{sign}(\tau_i^\alpha) = \begin{cases} -1 & \text{if } \tau_i^\alpha < 0, \\ 0 & \text{if } \tau_i^\alpha = 0, \\ 1 & \text{if } \tau_i^\alpha > 0. \end{cases}$$

2.9. Kinetic relations for species volume fraction

We use inequality (33)₂ to derive kinetic relations for species volume fractions. To impose the physical constraint $\sum_{i=1}^P \xi_i = 1 \Rightarrow \sum_{i=1}^P \dot{\xi}_i = 0$, we follow the work of Thamburaja and Jamshidian (2014) and define

¹ As the present study focuses on SIBM in BCC crystalline metals at relatively high temperatures, the part of the resistance due to athermal obstacles to slip is neglected and only the part due to thermally activated obstacles is considered (Kothari and Anand, 1998; Lim et al., 2015).

$$\dot{\xi}_i = \sum_{p < q} K_{ipq} \dot{\xi}_{pq} \quad \text{with } p = 1, 2, \dots, P-1 \quad \text{and } q = 2, 3, \dots, P \quad (38)$$

where, the kinetic variables $\dot{\xi}_{pq}$ are the *transformation/conversion rate* between species p and species q . The stoichiometric coefficients K_{ipq} are defined as

$$K_{ipq} = \begin{cases} 1 & \text{if } i = p \\ -1 & \text{if } i > p \text{ and } i = q \\ 0 & \text{otherwise} \end{cases}$$

to ensure the permanent compliance with the constraint $\sum_{i=1}^P \dot{\xi}_i = 0$ during inter-species conversions. Defining the *partial driving force* for inter-species conversions by

$$f_i^\xi = \text{Div } \mathbf{h}_i - \frac{\partial \psi}{\partial \xi_i} \quad \text{with } i = 1, 2, \dots, P, \quad (39)$$

and substituting Eq. (38) into inequality (33)₂ results in

$$\sum_{p < q} f_{pq}^\xi \dot{\xi}_{pq} \geq 0 \quad \text{with } p = 1, 2, \dots, P-1 \quad \text{and } q = 2, 3, \dots, P, \quad (40)$$

where $f_{pq}^\xi = f_p^\xi - f_q^\xi$ represents the total driving force for *inter-species conversion* between species p and q . To satisfy inequality (40) we assume that the dissipation accompanying the inter-species conversion between each species p and q with $p < q$ is strictly *non-negative*, and that each dissipation mechanism is also *strongly* dissipative i.e.

$$f_{pq}^\xi \dot{\xi}_{pq} > 0 \quad \text{for } \dot{\xi}_{pq} \neq 0. \quad (41)$$

Inequality (41) is satisfied by taking

$$\dot{\xi}_{pq} = \begin{cases} L_{pq}^\xi f_{pq}^\xi & \text{if } |\nabla \xi_p| > 0, |\nabla \xi_q| > 0, \text{ and } |f_{pq}^\xi| > f_{pq}^{\xi,c} \\ 0 & \text{otherwise,} \end{cases} \quad (42)$$

where the model parameters $L_{pq}^\xi = \hat{L}_{pq}^\xi(\theta) > 0$ represent *mobility-like* coefficients which control the kinetics of inter-species conversions, the material parameters $f_{pq}^{\xi,c} \geq 0$ denote the *thermodynamic resistance* to inter-species conversions between species p and q (Thamburaja and Jamshidian, 2014; Jamshidian et al., 2016). Substituting Eqs. (15) and (27) in Eq. (39) results in

$$f_i^\xi = f_i^m + f_i^e + f_i^\theta + f_i^d, \quad (43)$$

with the partial driving force due to grain boundary curvature

$$f_i^m = - \sum_{r \neq i}^P \frac{e_{ir}^\xi}{2} \mathbf{C}^{-1} : \nabla \nabla \xi_r - \sum_{r \neq i}^P \omega_{ir}^\xi \xi_r,$$

the partial driving forces arising from the heterogeneity in thermoelastic free energy

$$f_i^e = \frac{g'(\xi_i) \left[\sum_{r=1}^P g(\xi_r) (\psi_r^e - \psi_i^e) \right]}{\left[\sum_{r=1}^P g(\xi_r) \right]^2},$$

the partial driving force arising from the heterogeneity in purely thermal free energy

$$f_i^\theta = \frac{g'(\xi_i) \left[\sum_{r=1}^P g(\xi_r) (\psi_r^\theta - \psi_i^\theta) \right]}{\left[\sum_{r=1}^P g(\xi_r) \right]^2},$$

and finally the partial driving force caused by the heterogeneity in defect/plastic free energy

$$f_i^d = \frac{g'(\xi_i) \left[\sum_{r=1}^P g(\xi_r) (\psi_r^p - \psi_i^p) \right]}{\left[\sum_{r=1}^P g(\xi_r) \right]^2}.$$

To summarize, the list of material/model parameters that are to be calibrated/specified are

$$\left\{ K_1, K_2, h^{\alpha\beta}, C_d, b, \mu, \theta_0, \dot{\gamma}_0, m, \rho_{i,0}^\alpha, \mathcal{C}_i, \alpha_{th}, c_{th}, \varepsilon_{pq}^\xi, \omega_{pq}^\xi, L_{pq}^\xi, f_{pq}^{\xi,c} \right\}.$$

3. Computational homogenization

Following the works of [Thamburaja and Jamshidian \(2014\)](#) and [Jamshidian et al. \(2016\)](#), the constitutive theory has been implemented via a multiscale Taylor model-based computational procedure in which the macroscale deformation gradient $\bar{\mathbf{F}}$ applied to the material point represented by the RVE is assumed to be uniformly transmitted throughout the RVE i.e. $\mathbf{F} = \bar{\mathbf{F}}$. Also the mesoscale temperature throughout the RVE is supposed to be equal to the macroscale temperature i.e. $\theta = \bar{\theta}$.

In the multiscale coupled finite element and phase field computational procedure, the mesoscale kinetic relations are numerically implemented via phase field-like computations while the macroscale equilibrium is calculated by the finite element method in Abaqus/Standard. To conduct phase field computations, we have discretized the mesoscale domain of the RVE into Ω equal-volumed sub-domains. Using the Taylor model-based iso-strain assumption, the macroscale Cauchy stress $\bar{\mathbf{T}}$ at a finite element integration point as the macroscopic mechanical response of the material point represented by the RVE is given by ([Thamburaja and Jamshidian, 2014](#))

$$\bar{\mathbf{T}} = \frac{1}{\Omega} \sum_{k=1}^{\Omega} \mathbf{T}^k, \quad k = 1, 2, \dots, \Omega, \quad (44)$$

where \mathbf{T}^k is the Cauchy stress in the k -th subdomain of the RVE. Algorithmic details of the coupled finite element and phase field computational procedure are given in section 4.

4. Time integration procedure

Following [Thamburaja and Jamshidian \(2014\)](#), a multiscale sequentially-coupled staggered time integration procedure is developed for the numerical implementation of the constitutive theory. In our computational framework, the macroscopic stress-strain response of the material point is calculated by the finite-element method whereas the mesoscale microstructure evolution in the polycrystalline RVE due to SIBM is handled by phase field computations using finite difference method. The multiscale coupled finite-element and phase-field computational procedure has been implemented into the Abaqus/Standard finite element program by writing a user material subroutine UMAT. Algorithmic details of the time integration procedure are as follows.

We use ϕ as the finite-element integration point index where integers $\phi = 1, 2, \dots, \phi_{el}$ with ϕ_{el} being the total number of finite-element integration points. $k = 1, 2, \dots, \Omega$ is used as an index to represent the grid points of an RVE with Ω denoting the total number of grid points in the RVE.

Terminology and notation: A quantity at a grid point within an RVE (mesoscopic particle) is termed as a mesoscale quantity whereas a quantity at a finite-element integration point (macroscopic material point) is termed as a macroscale quantity. A quantity $\#$ at finite-element integration point ϕ is denoted by $\#^\phi$. A quantity $\#$ at the k -th grid point of the RVE attached to finite-element integration point ϕ is denoted by $\#^{\phi,k}$. A quantity $\#$ at the slip system α of k -th grid point of the RVE attached to finite-element integration point ϕ is characterized by $\#^{\phi,k,\alpha}$.

Treatment of microstructural variables: Recall that species i is present at a grid point if $0 < \xi_i \leq 1$, and that each species corresponds to a unique crystal orientation. In our numerical algorithm, we will only keep track of the species which exist at each grid point ([Kim et al., 2006; Thamburaja and Jamshidian, 2014](#)). Let set A_p represent the set that contains the species which satisfy the condition $0 < \xi_i \leq 1$ at a grid point. Furthermore, every member of set A_p is unique.

For our discussion in this paragraph, we will restrict our attention to the RVE attached to finite-element integration point ϕ : the k -th grid point of the RVE is labeled as $G^{\phi,k}$, and $G^{\phi,k}$ is located at position (x_1, x_2, x_3) in the reference configuration. The grid points located at positions $(x_1 + z, x_2, x_3)$, $(x_1 - z, x_2, x_3)$, $(x_1, x_2 + z, x_3)$, $(x_1, x_2 - z, x_3)$, $(x_1, x_2, x_3 + z)$ and $(x_1, x_2, x_3 - z)$ in the reference configuration are designated as the immediate neighboring grid points of $G^{\phi,k}$ with z being the grid spacing. The grid point index for each immediate neighboring grid point of $G^{\phi,k}$ is a member of set $Z^{\phi,k}$. Therefore, set $Z^{\phi,k}$ has six members. The j -th member of set $Z^{\phi,k}$ is denoted by $Z_j^{\phi,k}$ where integers $j = 1, 2, \dots, 6$. The integer label of each grid point, the coordinates of each grid point in the reference configuration and the integer labels for the immediate neighboring grid points of each grid point are obtained from an external file.

In the time integration procedure, we define t as the current time with $\Delta t > 0$ being an infinitesimal time increment, and $\tau = t + \Delta t$. We use the forward Euler method to perform the time integration of the grain growth equations. Using FORTRAN based statements, the algorithm for the time integration procedure is as follows:

DO $\phi = 1, \phi_{el}$ (Begin loop over the finite-element integration points)

- Given the macroscale quantities: $\{\bar{\mathbf{F}}^\phi(t), \bar{\mathbf{F}}^\phi(\tau), \bar{\theta}^\phi(t), \bar{\theta}^\phi(\tau), \bar{\mathbf{T}}^\phi(t), \bar{\rho}^\phi(t)\}$.
- Update the macroscale quantities (Steps A:C below): $\{\bar{\mathbf{T}}^\phi(\tau), \bar{\rho}^\phi(\tau)\}$.

DO $k = 1, \Omega$ (Begin loop over the grid points of the RVE)

- Given the mesoscale quantities: $\{\xi_i^{\phi,k}(t), A_p^{\phi,k}(t), Z^{\phi,k}, \rho_i^{\phi,k,\alpha}(t), \mathbf{F}_i^{p\phi,k}(t)\}$.
- Update the mesoscale quantities (Steps 1:13 below): $\{\xi_i^{\phi,k}(\tau), A_p^{\phi,k}(\tau), \rho_i^{\phi,k,\alpha}(\tau), \mathbf{F}_i^{p\phi,k}(\tau)\}$.

Step 1. Set the mesoscale deformation gradients $\mathbf{F}(t)$ and $\mathbf{F}(\tau)$:

$$\mathbf{F}(t) = \bar{\mathbf{F}}^\phi(t) \quad \text{and} \quad \mathbf{F}(\tau) = \bar{\mathbf{F}}^\phi(\tau).$$

Step 2. Set the mesoscale temperatures $\theta(t)$ and $\theta(\tau)$:

$$\theta(t) = \bar{\theta}^\phi(t) \quad \text{and} \quad \theta(\tau) = \bar{\theta}^\phi(\tau).$$

Step 3. Calculate the mesoscale right Cauchy-Green deformation tensor $\mathbf{C}(t)$:

$$\mathbf{C}(t) = \mathbf{F}^\top(t) \mathbf{F}(t).$$

Step 4. Determine the set A_ξ of species which are present at the grid point and its immediate neighbors:

$$A_\xi = \left[\cup_{j=1}^6 A_p^{\phi, Z_j^{\phi,k}}(t) \right] \cup A_p^{\phi,k}(t)$$

If $\text{card } A_\xi = 1$, no inter-species conversions can occur, and in this case we set $\xi_i^{\phi,k}(\tau) = \xi_i^{\phi,k}(t)$ for the species $i \in A_p^{\phi,k}(t)$, update $A_p^{\phi,k}(\tau) = A_p^{\phi,k}(t)$, and then proceed to Step 13.

Step 5. Calculate the mesoscale strain $\mathbf{E}_i^e(t)$ for each species $i \in A_\xi$:

$$\mathbf{F}_i^e(t) = \mathbf{F}(t) \left(\mathbf{F}_i^{p\phi,k}(t) \right)^{-1},$$

$$\mathbf{E}_i^e(t) = (1/2) \left\{ \left(\mathbf{F}_i^e(t) \right)^\top \mathbf{F}_i^e(t) - \mathbf{I} \right\}.$$

Step 6. Calculate the mesoscale free energies $\psi_i^e(t)$, $\psi_i^p(t)$ and $\psi_i^\theta(t)$ for each species $i \in A_\xi$:

$$\psi_i^e(t) = (1/2) \left\{ \mathbf{E}_i^e(t) - \alpha_{th} (\theta(t) - \theta_0) \mathbf{I} \right\} : \mathcal{E}_i [\mathbf{E}_i^e(t) - \alpha_{th} (\theta(t) - \theta_0) \mathbf{I}],$$

$$\psi_i^p(t) = a \mu b^2 \sum_{\alpha} \rho_i^{\phi,k,\alpha}(t),$$

$$\psi_i^\theta(t) = c_{th} [(\theta(t) - \theta_0) - \theta(t) \ln(\theta(t)/\theta_0)].$$

Step 7. Calculate the partial driving force for inter-species conversions, $f_i^\xi(t)$ for each species $i \in A_\xi$:

$$f_i^\xi(t) = f_i^m(t) + f_i^e(t) + f_i^\theta(t) + f_i^d(t),$$

where

$$f_i^m(t) = - \sum_{r \in A_\xi} \frac{\epsilon_{ir}^\xi}{2} \mathbf{C}^{-1}(t) : \nabla \nabla \xi_r^{\phi,k}(t) - \sum_{r \in A_\xi} \omega_{ir}^\xi \xi_r^{\phi,k}(t) \quad \text{with} \quad r \neq i,$$

$$f_i^e(t) = \frac{g'(\xi_i^{\phi,k}(t)) \left[\sum_{r \in A_\xi} g(\xi_r^{\phi,k}(t)) (\psi_r^e(t) - \psi_i^e(t)) \right]}{\left[\sum_{r \in A_\xi} g(\xi_r^{\phi,k}(t)) \right]^2},$$

$$f_i^\theta(t) = \frac{g'(\xi_i^{\phi,k}(t)) \left[\sum_{r \in A_\xi} g(\xi_r^{\phi,k}(t)) (\psi_r^\theta(t) - \psi_i^\theta(t)) \right]}{\left[\sum_{r \in A_\xi} g(\xi_r^{\phi,k}(t)) \right]^2},$$

$$f_i^d(t) = \frac{g'(\xi_i^{\phi,k}(t)) \left[\sum_{r \in A_\xi} g(\xi_r^{\phi,k}(t)) (\psi_r^p(t) - \psi_i^p(t)) \right]}{\left[\sum_{r \in A_\xi} g(\xi_r^{\phi,k}(t)) \right]^2}.$$

Note that $\xi_r^{\phi,k}(t) = 0$ if $i \notin A_p^{\phi,k}(t)$. The finite difference method for the calculation of the second gradient of phase field variables has been described in [Jamshidian et al. \(2014\)](#).

Step 8a. Calculate the total driving force for inter-species conversions, $f_{pq}(t)$ for species $p, q \in A_\xi$ with $p < q$:

$$f_{pq}(t) = f_p^\xi(t) - f_q^\xi(t).$$

Step 8b. Calculate the transformation rate increment between species, $\Delta \xi_{pq}$ for species $p, q \in A_\xi$ with $p < q$:

- If $|f_{pq}(t)| > f_{pq}^{\xi,c}$, then

$$\Delta \xi_{pq} = L_{pq}^\xi(t) f_{pq}(t) \Delta t.$$

The mobility coefficient, $L_{pq}^\xi(t) = \widehat{L}_{pq}^\xi(\theta(t))$.

- If $|f_{pq}(t)| < f_{pq}^{\xi,c}$, then

$$\Delta \xi_{pq} = 0.$$

Let set A_ξ denote the set containing the quantities $\Delta \xi_{pq} \neq 0$ for species $p, q \in A_\xi$ with $p < q$. If $A_\xi = \emptyset$, we set $\xi_i^{\phi,k}(\tau) = \xi_i^{\phi,k}(t)$ for each species $i \in A_p^{\phi,k}(t)$, update $A_p^{\phi,k}(\tau) = A_p^{\phi,k}(t)$; and then proceed to Step 13.

Step 9. Update the species volume fraction, $\xi_i^{\phi,k}(\tau)$ for each species $i \in A_\xi$:

$$\xi_i^{\phi,k}(\tau) = \xi_i^{\phi,k}(t) + \sum_{p < q} K_{ipq} \Delta \xi_{pq}, \quad p, q \in A_\xi.$$

If $\xi_i^{\phi,k}(\tau) > 1$ then set $\xi_i^{\phi,k}(\tau) = 1$ and if $\xi_i^{\phi,k}(\tau) < 0$, then set $\xi_i^{\phi,k}(\tau) = 0$.

Step 10. Update the set $A_p^{\phi,k}(\tau)$ of species which satisfy:

$$0 < \xi_i^{\phi,k}(\tau) \leq 1, \quad i \in A_\xi.$$

Step 11. Ensure that the constraint $\sum_{i \in A_p^{\phi,k}(\tau)} \xi_i^{\phi,k}(\tau) = 1$ is satisfied by replacing

$$\xi_i^{\phi,k}(\tau) \quad \text{with} \quad \frac{\xi_i^{\phi,k}(\tau)}{\sum_{r \in A_p^{\phi,k}(\tau)} \xi_r^{\phi,k}(\tau)}, \quad i \in A_p^{\phi,k}(\tau).$$

Step 12. The dislocation reduction behind a moving grain boundary if $(\xi_i^{\phi,k}(\tau) - \xi_i^{\phi,k}(t)) > 0$ for each species $i \in A_\xi$:

$$\rho_i^{\phi,k,\alpha}(\tau) = \rho_i^{\phi,k,\alpha}(t) - \rho_i^{\phi,k,\alpha}(t) C_d \left(\xi_i^{\phi,k}(\tau) - \xi_i^{\phi,k}(t) \right).$$

Step 13. Update the mesoscale Cauchy stress $\mathbf{T}_i^{\phi,k}(\tau)$ for each species $i \in A_\xi$:

Step 13-1. Calculate

$$\mathbf{F}_i^{e,trial} = \mathbf{F}(\tau) \left(\mathbf{F}_i^{p^{\phi,k}}(t) \right)^{-1},$$

$$\mathbf{C}_i^{e,trial} = \left(\mathbf{F}_i^{e,trial} \right)^\top \mathbf{F}_i^{e,trial},$$

$$\mathbf{E}_i^{e,trial} = \frac{1}{2} \left(\mathbf{C}_i^{e,trial} - \mathbf{I} \right),$$

$$\mathbf{T}_i^{e,trial} = \mathcal{E}_i \left[\mathbf{E}_i^{e,trial} - \alpha_{th} (\theta(\tau) - \theta_0) \mathbf{I} \right].$$

Step 13-2. Solve the following three coupled equations for calculating $\Delta \gamma_i^\alpha \equiv \dot{\gamma}_i^\alpha \Delta t$ for each slip system α :

$$\mathbf{T}_i^{\phi,k}(\tau) = \mathbf{T}_i^{e,trial} - \sum_{\alpha} \Delta \gamma_i^\alpha \mathbf{C}_i^\alpha,$$

$$s_i^{\phi,k,\alpha}(\tau) = \mu b \sqrt{\sum_{\beta} h^{\alpha\beta} \rho_i^{\phi,k,\beta}(\tau)},$$

$$\rho_i^{\phi,k,\alpha}(\tau) = \rho_i^{\phi,k,\alpha}(t) + K_1 \sqrt{\rho_i^{\phi,k,\alpha}} |\Delta \gamma_i^\alpha| - K_2 \rho_i^{\phi,k,\alpha} \Delta t,$$

with $\mathbf{C}_i^\alpha = \mathcal{E}_i[\text{sym}(\mathbf{C}_i^{e,trial} \mathcal{S}_{i,0}^\alpha)]$ for each species i in $A_p^{\phi,k}(\tau)$, where $\mathcal{S}_{i,0}^\alpha = (\mathbf{s}_{i,0}^\alpha \otimes \mathbf{m}_{i,0}^\alpha)$. For calculating $\mathbf{T}_i^{\phi,k}(\tau)$, $s_i^{\phi,k,\alpha}(\tau)$ and $\rho_i^{\phi,k,\alpha}(\tau)$ we use the following three-level iterative procedure.

At the first level, by using a Newton-type iterative algorithm, the first equation is solved for $\mathbf{T}_i^{\phi,k}(\tau)$, while $s_i^{\phi,k,\alpha}(\tau)$ and $\rho_i^{\phi,k,\alpha}(\tau)$ are fixed at their best available estimates. Estimates of $\mathbf{T}_i^{\phi,k}(\tau)$ at the end of n and $n+1$ iterations of Newton-Raphson are identified by subscripts n and $n+1$, respectively.

$$\mathbf{T}_{i,n+1}^{\phi,k}(\tau) = \mathbf{T}_{i,n}^{\phi,k}(\tau) - \mathcal{J}_{i,n}^{-1} [\mathbf{G}_{i,n}],$$

with

$$\mathbf{G}_{i,n} \equiv \mathbf{T}_{i,n}^{\phi,k}(\tau) - \mathbf{T}_i^{e,trial} + \sum_{\alpha} \Delta \gamma_i^\alpha \left(\mathbf{T}_{i,n}^{\phi,k}(\tau), \mathbf{s}_{i,r}^{\phi,k,\alpha}(\tau), \rho_{i,m}^{\phi,k,\alpha}(\tau) \right) \mathbf{C}_i^\alpha,$$

$$\mathcal{J}_{i,n} \equiv \mathcal{J}_i + \sum_{\beta} \mathbf{C}_i^\alpha \otimes \frac{\partial}{\partial \mathbf{T}_{i,n}^{\phi,k}(\tau)} \Delta \gamma_i^\alpha \left(\mathbf{T}_{i,n}^{\phi,k}(\tau), \mathbf{s}_{i,r}^{\phi,k,\alpha}(\tau), \rho_{i,m}^{\phi,k,\alpha}(\tau) \right).$$

At the second level, while $s_i^{\phi,k,\alpha}(\tau)$ is fixed at its best available estimate, $\rho_i^{\phi,k,\alpha}(\tau)$ is updated as follows:

$$\rho_{i,m+1}^{\phi,k,\alpha}(\tau) = \rho_i^{\phi,k,\alpha}(t) + K_1 \sqrt{\rho_{i,m}^{\phi,k,\alpha}} \left| \Delta \gamma_i^\alpha \left(\mathbf{T}_{i,n+1}^{\phi,k}(\tau), \mathbf{s}_{i,r}^{\phi,k,\alpha}(\tau), \rho_{i,m}^{\phi,k,\alpha}(\tau) \right) \right| - K_2 \rho_{i,m}^{\phi,k,\alpha} \Delta t,$$

where the value of $\rho_i^{\phi,k,\alpha}(\tau)$ at the end of the m th update at the second level is identified by the subscript m .

At the third level, $s_i^{\phi,k,\alpha}(\tau)$ is updated by:

$$s_{i,r+1}^{\phi,k,\alpha}(\tau) = \mu b \sqrt{\sum_{\beta} h^{\alpha\beta} \rho_{i,m+1}^{\phi,k,\beta}(\tau)}$$

where the value of $s_i^{\phi,k,\alpha}(\tau)$ at the end of the r th update at the third level is shown by the subscript r .

Step 13-3. Calculate

$$\mathbf{F}_i^{p\phi,k}(\tau) = \left\{ \mathbf{I} + \sum_{\alpha} \Delta \gamma_i^{\alpha} \mathcal{S}_{i,0}^{\alpha} \right\} \mathbf{F}_i^{p\phi,k}(t).$$

We then normalize $\mathbf{F}_i^{p\phi,k}(\tau)$ in order to make sure that the determinant of $\mathbf{F}_i^{p\phi,k}(\tau)$ remains unity. To normalize $\mathbf{F}_i^{p\phi,k}(\tau)$, the computed values of its components are divided by the cube root of its computed determinant.

Step 13-4. Calculate

$$\mathbf{T}_i^{\phi,k}(\tau) = \frac{1}{\det \mathbf{F}(\tau)} \mathbf{F}(\tau) \left(\mathbf{F}_i^{p\phi,k}(\tau) \right)^{-1} \mathbf{T}_i^{p\phi,k}(\tau) \left(\mathbf{F}_i^{p\phi,k}(\tau) \right)^{-\top} \mathbf{F}^{\top}(\tau).$$

Step 13-5. Calculate the mesoscale Cauchy stress $\mathbf{T}^{\phi,k}(\tau)$ and $\rho^{\phi,k}(\tau)$ for each grid point:

$$\mathbf{T}^{\phi,k}(\tau) = \frac{\sum_{i \in A_p^{\phi,k}(\tau)} g(\xi_i^{\phi,k}(\tau)) \mathbf{T}_i^{\phi,k}(\tau)}{\sum_{i \in A_p^{\phi,k}(\tau)} g(\xi_i^{\phi,k}(\tau))},$$

$$\rho^{\phi,k}(\tau) = \frac{\sum_{i \in A_p^{\phi,k}(\tau)} \sum_{\alpha} g(\xi_i^{\phi,k}(\tau)) \rho_i^{\phi,k,\alpha}(\tau)}{\sum_{i \in A_p^{\phi,k}(\tau)} g(\xi_i^{\phi,k}(\tau))}.$$

END DO (End loop over the grid points of the RVE)

Step A. Update the macroscale Cauchy stress, using Eq. (44):

$$\bar{\mathbf{T}}^{\phi}(\tau) = \frac{1}{\Omega} \sum_{k=1}^{\Omega} \mathbf{T}^{\phi,k}(\tau).$$

Step B. Calculate the macroscale dislocation density:

$$\bar{\rho}^{\phi}(\tau) = \frac{1}{\Omega} \sum_{k=1}^{\Omega} \rho^{\phi,k}(\tau).$$

Step C. To determine the Jacobian matrix for the finite-element code Abaqus/Standard to perform Newton-Raphson iterations, the combination of analytical Jacobian of Balasubramanian (1998) and Thamburaja and Jamshidian (2014) was used.

END DO (End loop over the finite-element integration points).

5. Results and discussion

In this section, the developed constitutive theory and numerical algorithm are used for simulating dynamic SIBM in tantalum. The evolution of microstructure via SIBM in bicrystalline and polycrystalline tantalum samples under thermo-mechanical loading is investigated. The bicrystalline simulations are conducted to analyze the migration of a flat boundary as the simplest case study. Simulations of SIBM in a polycrystalline RVE are performed to primarily demonstrate the ability of the constitutive model for predicting the experimental data available in the literature and secondly to further investigate SIBM. Before presenting the numerical simulation results, the experiments of Pedrazas et al. (2014) on SIBM in polycrystalline tantalum are briefly described as follows.

Pedrazas et al. (2014) conducted high-temperature simple-tension experiments on tantalum polycrystalline dog-bone sheet samples of thickness 760 μm under strain-controlled conditions to produce large single crystals by dynamic SIBM. The solid line in Fig. 2a shows the experimental stress-strain response of the tantalum polycrystal at the fixed true-strain rate of $5 \times 10^{-4} \text{ s}^{-1}$ and temperature of 2123 K. The average grain size of the polycrystalline sample at the onset of deformation was 570 μm . During the simple tension test, when the tensile strain reaches a *critical strain*, SIBM occurs at a few specific grains in the polycrystalline sample. As shown in Fig. 2, initiation of SIBM causes a sudden drop in the flow stress. While the strain at a constant true strain rate is being applied to the specimen, the growth of these grains by SIBM results in further reduction of flow stress. The decrease of flow stress during SIBM is attributed to the reduction of the dislocation content behind the moving grain boundaries and the associated change in texture which in turn cause local softening of the material.

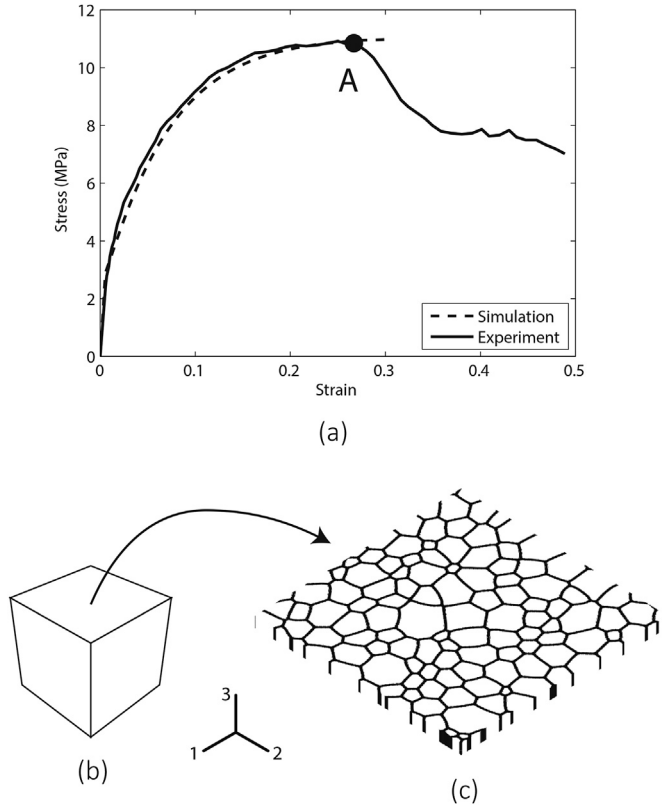


Fig. 2. (a) The solid line shows the experimental stress-strain response (Pedrazas et al., 2014) of tantalum polycrystal under uniaxial tensile true-strain rate $5 \times 10^{-4} \text{ s}^{-1}$ at temperature 2123 K and the dashed line represents the numerically simulated stress-strain response fitted to the experimental result until point A i.e. before the initiation of SIBM. (b) A cubic C3D8R type finite element with a single integration point at its centroid at the macroscale under uniaxial tensile loading along direction 1 and (c) the tantalum polycrystalline RVE at the mesoscale attached to the integration point of the finite element.

Pedrazas et al. (2014) have reported that SIBM initiates at a critical strain of 0.266 and a corresponding stress value of 10.90 MPa for the case of polycrystalline tantalum. Also, they have emphasized the necessity of plastic straining for SIBM propagation after initiation.

To perform numerical simulations of SIBM using the multiscale coupled finite element and phase field computational procedure, the computational model of tantalum polycrystalline RVE is created as follows. The multiscale model is composed of (i) a single Abaqus three-dimensional continuum finite-element with reduced integration C3D8R which is an 8-node linear brick element with a single integration point at its centroid at the macroscale as shown in Fig. 2b and (ii) a connected phase field polycrystalline RVE with diffuse interfaces at the mesoscale as shown in Fig. 2c. Such a single-RVE multiscale model is sufficient to simulate SIBM in a material point situated within the gage length of the dog-bone tantalum samples under uniform tensile deformation (Jamshidian et al., 2016). Since the thickness of the experimental polycrystalline tantalum sheet sample ($760 \mu\text{m}$) and its average grain size ($570 \mu\text{m}$) are comparable, we follow the work of Jamshidian et al. (2016) on stressed grain growth in polycrystalline thin films and assume a columnar polycrystalline microstructure of the RVE for simplicity and computational efficiency. Also, the initial random texture of the RVE is created by assigning a random orientation to each grain by the method described in the work of Anand (2004). The RVE in Fig. 2c is discretized over $400 \times 400 \times 1$ grid points along axes 1, 2 and 3, respectively with uniform grid spacing of $z = 14 \mu\text{m}$ and a diffuse interface thickness of $\tilde{\ell} = 6z$. The RVE contains approximately 106 grains with the average grain diameter $570 \mu\text{m}$ as in the experiments. Periodic boundary conditions are applied for the phase field variables on the external boundaries of the RVE.

As in the experiments, a uniaxial tensile deformation in direction 1 is applied to the finite element using a prescribed displacement boundary condition with a constant strain rate of $5 \times 10^{-4} \text{ s}^{-1}$ at temperature 2123 K as shown in Fig. 2b. To apply a constant strain rate $\dot{\epsilon}$, the following velocity boundary condition is applied to the finite element in direction 1:

$$v = h \dot{\epsilon} \exp(\dot{\epsilon} t),$$

where h is the height of the finite element along direction 1 and t is time. This velocity boundary condition is implemented in Abaqus by writing a user-amplitude subroutine.

5.1. Determination of material parameters for single crystal tantalum

The elastic modulus tensor \mathcal{C}_k for each species k is determined by its crystallographic orientation and the three elastic constants C_{11} , C_{12} and C_{44} of tantalum crystal with cubic symmetry. The values of the elastic constants for tantalum as a function of temperature are (Simmons and Wang, 1971; Kothari and Anand, 1998)

$$\begin{aligned} C_{11} &= (268.2 - 0.024 \theta) \text{ GPa} \\ C_{12} &= (159.6 - 0.011 \theta) \text{ GPa} \\ C_{44} &= (87.1 - 0.015 \theta) \text{ GPa} \end{aligned} \quad (45)$$

and the shear modulus for cubic crystal is given by

$$\mu = \sqrt{(C_{44} \times (C_{11} - C_{12})/2)}.$$

For the modeling of plastic deformation due to crystallographic slip in tantalum with BCC lattice structure, the 24 slip systems $\{110\} \langle 111 \rangle$ and $\{112\} \langle 111 \rangle$ are considered and any small asymmetry of slip on the $\{112\}$ planes is neglected (Kothari and Anand, 1998).

The magnitude of the Burgers vector and the coefficient of thermal expansion taken from literature are $b = 2.92 \text{ \AA}$ and $\alpha_{th} = 6.3 \times 10^{-6} \text{ K}^{-1}$, respectively. The typical values selected for the initial dislocation density, the constant reference strain-rate and the constant-rate sensitivity parameter are respectively $\rho_0^\alpha = 0.04 \mu\text{m}^{-2}$, $\dot{\gamma}_0^\alpha = 10.0 \text{ s}^{-1}$ and $m = 0.3$. Also, a simple isotropic form is considered for the hardening parameters in Eq. (36) i.e. we set $h^{\alpha\beta} = 1$. Following the work of Abrivard et al. (2012a), we set $C_d = 5$.

Referring back to the evolution law for dislocation densities in Eq. (17), the dislocation-accumulation modulus K_1 and recovery modulus K_2 are calibrated by fitting the simulated stress-strain response of the polycrystalline RVE shown in Fig. 2c to the experimental stress-strain response of polycrystalline tantalum before the initiation of SIBM at point A in Fig. 2a. During simulations, SIBM is prevented by suppressing the evolution of phase field variables. The numerically simulated stress-strain response fitted to the experiments is shown by the dashed line in Fig. 2a using the fitting parameters $K_1 = 193 \mu\text{m}^{-1}$ and $K_2 = 0.014 \text{ s}^{-1}$.

5.2. Determination of model parameters for grain boundary migration

Following the work of Kim et al. (2006), the grain boundary related model parameters $\{\varepsilon_{pq}^\xi, \omega_{pq}^\xi, L_{pq}^\xi\}$ have definite relationships with the diffuse grain boundary thickness \tilde{l}_{pq}^ξ , grain boundary mobility M_{pq} and grain boundary energy γ_{pq}^ξ between species p and q as

$$\omega_{pq}^\xi = \frac{4 \gamma_{pq}^\xi}{\tilde{l}_{pq}^\xi}, \quad \varepsilon_{pq}^\xi = \frac{8}{\pi^2} \gamma_{pq}^\xi \tilde{l}_{pq}^\xi, \quad L_{pq}^\xi = \frac{\pi^2}{8} \frac{M_{pq}}{\tilde{l}_{pq}^\xi}, \quad (46)$$

where $M_{pq} = M_{pq}^\circ \exp(-G_{pq}/K_b \theta)$ with K_b being the Boltzmann constant and the material parameters $M_{pq}^\circ > 0$ and $G_{pq} > 0$ denoting the reference mobility and activation energy, respectively.

For simplicity, we assume isotropic grain boundary properties (Jamshidian and Rabczuk, 2014; Tonks and Millett, 2011) and set $\gamma_{pq}^\xi = \gamma^\xi \equiv \text{constant}$, $M_{pq}^\circ = M^\circ \equiv \text{constant}$, $G_{pq} = G \equiv \text{constant}$ which means that grain boundary properties are independent of the grain boundary misorientation angle. The diffuse grain boundary thickness is also taken to be the same for all grain boundaries i.e. $\tilde{l}_{pq}^\xi = \tilde{l}^\xi \equiv \text{constant}$. These assumptions result in $\omega_{pq}^\xi = \omega^\xi \equiv \text{constant}$, $\varepsilon_{pq}^\xi = \varepsilon^\xi \equiv \text{constant}$, $M_{pq} = M \equiv \text{constant}$ and $L_{pq}^\xi = L^\xi \equiv \text{constant}$.

We use the following typical values available in the literature for tantalum grain boundary energy and mobility

$$\gamma^\xi = 1.2 \text{ J m}^{-2}, \quad M = 2.72 \times 10^{-9} \text{ m}^4 \text{ J}^{-1} \text{ s}^{-1},$$

and use Eqs. (46) to get

$$\omega^\xi = 0.057 \text{ MJ m}^{-3}, \quad \varepsilon^\xi = 81.71 \mu\text{J m}^{-1}, \quad L^\xi = 40 \mu\text{J}^{-1} \text{ m}^3 \text{ s}^{-1}.$$

Finally, following Thamburaja and Jamshidian (2014) we assume that the thermodynamic resistance to inter-species conversions is a constant parameter independent of grain boundary misorientation angle i.e. we assume $f_{pq}^{\xi,c} = f^c \equiv \text{constant}$ where f^c is a constant material parameter representing the volumetric resistance (units of energy per unit volume) to grain boundary migration.

Before conducting numerical simulation for SIBM in polycrystalline tantalum, we use the aforementioned material and model parameters to perform SIBM simulations for a flat boundary in a tantalum bicrystalline specimen.

5.3. Analysis of SIBM in a tantalum bicrystalline RVE

Experimental studies on SIBM in bicrystals (Theyssier and Driver, 1999; Kashiwara et al., 2011) have shown that when a bicrystalline specimen composed of two differently oriented single crystals separated by a flat boundary is deformed by plane strain compression or rolling at high temperature, the two grains acquire different stored energy values. In response to this stored energy difference across the grain boundary, SIBM occurs resulting in the growth of the grain with lower stored energy.

In this section, we use the developed constitutive model and the material parameters determined in sections 5.1 and 5.2 to simulate SIBM in a bicrystalline RVE. As shown in Fig. 3a, the bicrystal consists of two grains with $\langle 001 \rangle$ and $\langle 111 \rangle$ orientations separated by a planar flat boundary. These orientations have been selected as they demonstrate a large hardening difference under deformation and consequently produce a large stored energy difference across the grain boundary. As the grain boundary is flat, the curvature driving force is absent in this specific case study. Also, the critical resistance to grain boundary migration is not considered in this case study i.e. $f^c = 0$. The SIBM simulation begins by applying a uniaxial tensile loading in direction 1 to the finite element representing the bicrystalline RVE with a constant strain rate of $5 \times 10^{-4} \text{ s}^{-1}$ at temperature 2123 K.

Shown in Fig. 3b is the numerically simulated stress-strain response of the bicrystalline RVE. Also, the evolution of the macroscale dislocation density in the bicrystal in terms of the applied strain is shown in Fig. 4. The contour plots of the dislocation density distribution within the tantalum bicrystalline microstructure are plotted in Fig. 5 at different strain values labeled by points A, B, C and D in Fig. 4. These points are respectively corresponding to the strain values 0.018, 0.108, 0.18 and 0.261. These plots illustrate the evolution of dislocation density within the microstructure during dynamic SIBM.

By the application of tensile loading to the bicrystal at constant strain rate, both the flow stress and the macroscale dislocation density increase with strain. Under the applied loading conditions, the $\langle 100 \rangle$ oriented crystal acquires less stored deformation energy compared to the $\langle 111 \rangle$ oriented crystal; resulting in a stored energy difference across the grain

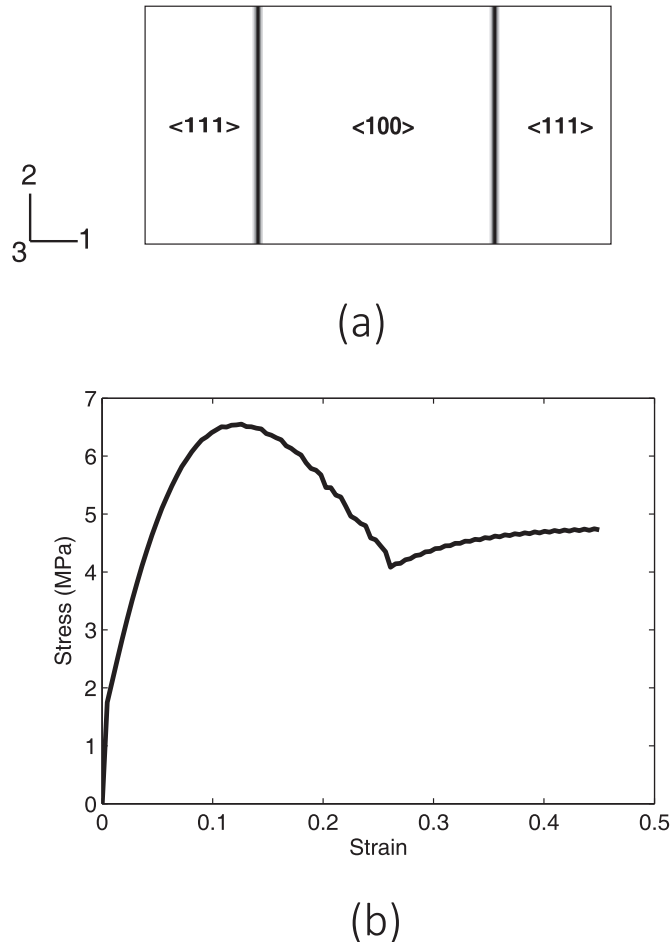


Fig. 3. (a) tantalum bicrystalline RVE used in numerical simulations. (b) Numerically simulated stress-strain response of the bicrystal under uniaxial tensile loading in direction 1 with a constant strain rate.

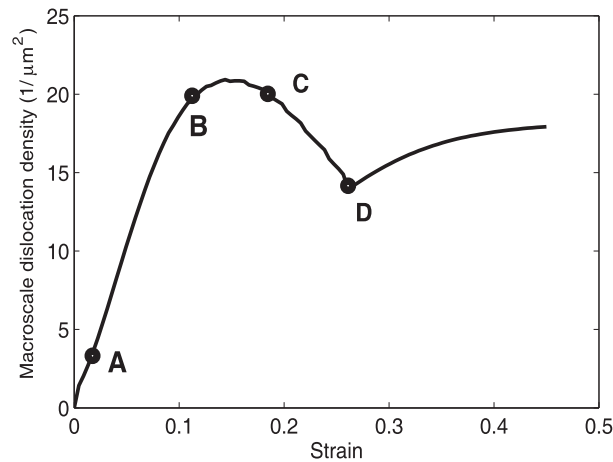


Fig. 4. The evolution of the macroscale dislocation density in the bicrystal in terms of the applied macroscale strain. The points labeled as A, B, C and D are respectively corresponding to the strain values 0.018, 0.108, 0.18 and 0.261.

boundary separating the two crystals. At point A in Fig. 4 while the total dislocation density has increased to some perceptible values, the stored energy difference is not enough to cause a sensible movement of grain boundary as shown in the contour plot A in Fig. 5a. By further straining of the bicrystal, the stored energy difference across the grain boundary rises and eventually provides sufficient driving force to initiate SIBM as shown in Fig. 5b.

Initiation of SIBM is identified by point B in Fig. 4. By the onset of grain boundary migration by SIBM, the increasing rate of the flow stress and macroscale dislocation density gradually decrease beyond point B. Continuous straining of the bicrystal further increases the stored energy difference across the grain boundary, resulting in the acceleration of SIBM between points B and C in Fig. 4. Due to the reduction of the dislocation density behind the migrating grain boundary by SIBM, the rate of change of the flow stress and the macroscale dislocation density gradually decreases to become negative at some point between B and C. In other words, the occurrence of SIBM at the mesoscale, converts the increasing rate of the flow stress and macroscale dislocation density at point B to a decreasing rate at point C. As shown in the contour plot of the dislocation density in Fig. 5c, at point C the boundary has moved over a finite distance and the dislocation density has decreased behind it. Also, this figure shows that while the dislocation density decreases behind the moving grain boundary, it is untouched in its front. However, further continuous straining causes the increase of the dislocation density in both rear and front of the moving grain boundary.

The consequence of the competing decrease of the dislocation density due to SIBM and increase of the dislocation density due to straining is the reduction of the macroscale dislocation density and flow stress beyond point C in Fig. 4. This reduction persists by the continuation of SIBM until the expanding $\langle 100 \rangle$ crystal totally consumes the shrinking $\langle 111 \rangle$ crystal and the whole mesoscale domain becomes a single Crystal with $\langle 100 \rangle$ orientation at point D in Fig. 4. By the completion of SIBM at point D, further straining results in the hardening of the single crystalline domain and consequently the increase of macroscale dislocation density and flow stress beyond point D.

In order to have a closer look at the evolution of the local dislocation density values within the bicrystal during SIBM at the mesoscale, the profile of dislocation density along the bicrystal in direction 1 is plotted in Fig. 6 at different strain values identified by points B, C and D in Fig. 4. Fig. 6 clearly shows the sudden decrease of dislocation density behind the moving grain boundary due to SIBM and also the gradual increase of dislocation density far away from the moving grain boundary due to continuous straining.

The aforementioned results agree with experimental TEM observations of discontinuous dynamic recrystallization in polycrystalline copper (Sakai et al., 2014) and also recent SIBM simulation results (Zhao et al., 2017). These previous studies have shown that SIBM leaves a low-dislocation density region behind the migrating grain boundary and new dislocations are accumulated far away from the mobile grain boundary.

5.4. Simulation of SIBM in tantalum polycrystalline RVE and comparison with experiments

In this section, the developed constitutive model and the material parameters determined in sections 5.1 and 5.2 are employed to simulate SIBM in the tantalum polycrystalline RVE shown in Fig. 2c. SIBM simulations in the polycrystal begin by the application of the previously-described uniaxial tension with a constant strain rate along direction 1. The numerically-simulated stress-strain response of the tantalum polycrystalline RVE is shown by the solid line in Fig. 7a where the experimental response is also drawn by the dashed line for comparison. In addition, the evolution of the macroscale dislocation density in the polycrystal as a function of the applied macroscale strain is shown in Fig. 7b. The contour plots of dislocation density distribution within the tantalum polycrystalline microstructure are displayed in Fig. 8 at different strain values

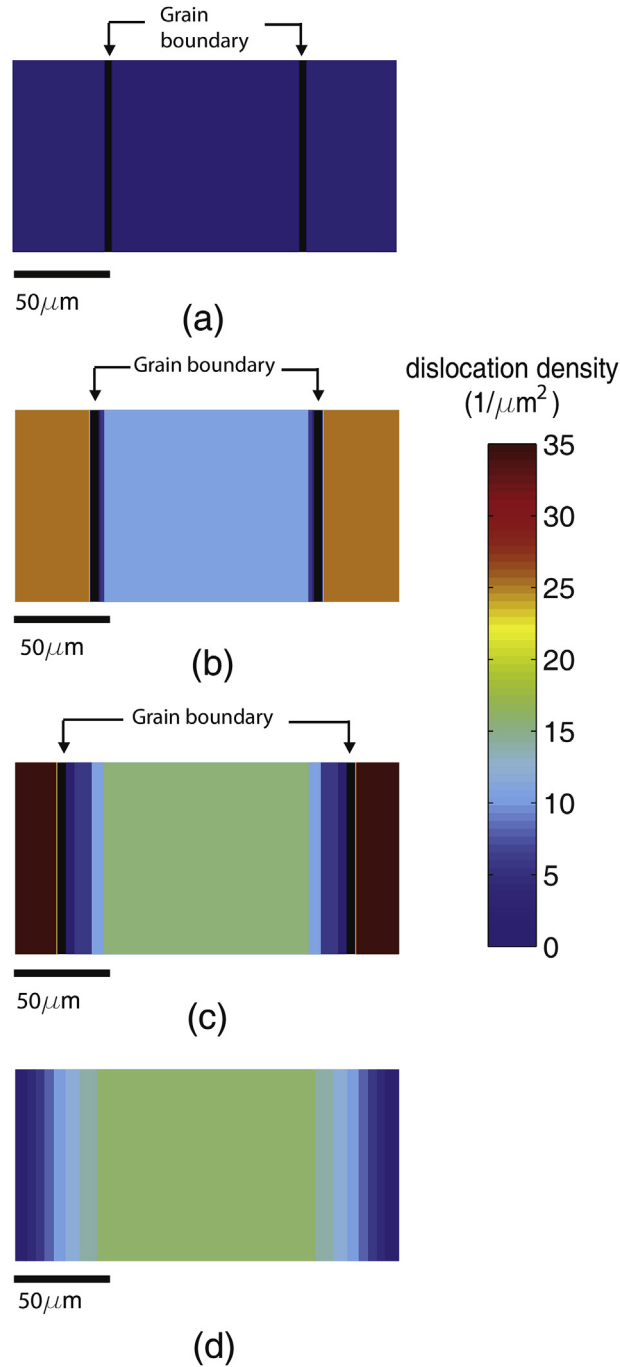


Fig. 5. The contour plots of dislocation density in the tantalum bicrystalline microstructure at different strain values labeled by points (a) A, (b) B, (c) C and (d) D in Fig. 4.

labeled by points A, B, C, D, E, and F in Fig. 7a. These points are respectively corresponding to the macroscale strain values 0.00, 0.24, 0.26, 0.32, 0.35 and 0.40. Zero strain at point A corresponds to the undeformed state. These plots demonstrate the evolution of dislocation density within the polycrystalline microstructure during dynamic SIBM. In order to have a statistical analysis of the evolution of grain sizes during SIBM, the grain size distribution (GSD) histograms for the initial undeformed microstructure and the final microstructure, respectively, labeled by points A and F in Fig. 7a are plotted in Fig. 9.

During the simulations, at a specific strain level the local value of the stored energy difference at a particular grain boundary segment within the RVE reaches and overcomes the critical resistance to grain boundary migration, leading to SIBM. Initiation and propagation of SIBM is characterized by a sudden and continuous drop in the stress-strain response of the

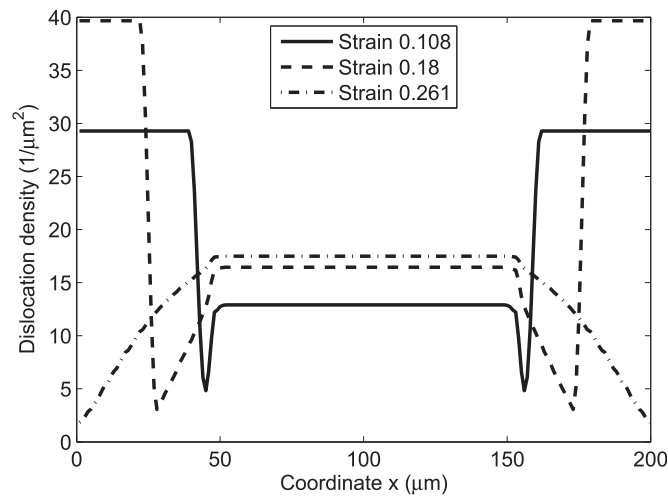


Fig. 6. The profile of dislocation density in the tantalum bicrystal shown in Fig. 3a along direction 1 at different strain values identified by points B, C and D in Fig. 4.

polycrystalline RVE as shown in Fig. 7a between points B and C. Our simulations have shown that the specific strain level for the initiation of SIBM is directly related to the critical resistance to grain boundary migration identified by the material parameter f^c . Particularly, increasing f^c postpones the initiation of SIBM to higher strain values. In our simulations, the value of f^c has been chosen so that SIBM initiates at the same strain level as in the experiments (Pedrazas et al., 2014). The simulated stress-strain response in Fig. 7a is obtained using $f^c = 0.052 \text{ MJ m}^{-3}$. As shown in Fig. 7a, the numerical simulation results show a satisfactory correspondence with the experimental data after the initiation of SIBM beyond point B.

Analysis of the simulation results presented in Figs. 7–9 suggests the following trends:

Trend 1: A minimum critical macroscopic strain value for the initiation of SIBM is observed. Before reaching this critical strain, SIBM does not occur as the local values of the stored energy difference across grain boundary segments within the mesoscale microstructure are below the critical resistance to grain boundary migration. The critical strain for the mesoscale initiation of SIBM is identified by point B in Fig. 7a and the corresponding contour plot for the distribution of mesoscale dislocation density is shown in Fig. 8b.

Trend 2: By further increasing the macroscopic strain beyond the critical strain for the initiation of SIBM, at a specific grain boundary segment the local value of the stored energy difference reaches the critical resistance for grain boundary migration while the stored energy difference elsewhere is still below the critical resistance. As a result, this specific grain boundary segment migrates by SIBM. The macroscale manifestation of SIBM is identified by point C in Fig. 7a and the corresponding contour plot for the distribution of mesoscale dislocation density is shown in Fig. 8c. The stress-strain response in Fig. 7a demonstrates a sudden drop in the macroscopic flow stress due to the initiation of SIBM. The contour plot in Fig. 8c clearly shows the reduction of the dislocation density behind the migrating grain boundary by SIBM.

Trend 3: Within a finite period of time, SIBM is continued by the same grain boundary segment at which SIBM was initiated, as shown in Fig. 8d. This is due to the reduction of the dislocation density behind the moving grain boundary and consequently the intensification of the driving force due to the stored energy difference. The reduction of the dislocation density in the region swept by the moving grain boundary results in the reduction of the total dislocation density within the RVE and consequently the reduction of the macroscale flow stress, as shown in point D in Fig. 7a. By the persisting increase of the applied strain under constant strain rate, the local value of stored energy difference reaches the critical resistance for grain boundary migration at some other specific grain boundary segments and consequently SIBM initiates at some other locations within the microstructure, as shown in Fig. 8d.

Trend 4: The so-called abnormal grains grown by SIBM are impeded by the low stored energy grains. Particularly, when a grain growing by SIBM encounters a relatively low stored energy grain, SIBM stops due to the fall of the driving force below the critical resistance for grain boundary migration. As shown in Fig. 8e, such impeding grains are observed as island grains surrounded by the abnormal grains grown by SIBM.

Trend 5: As in the experimental stress-strain curve, the simulated stress response under a constant strain rate shown in Fig. 7a demonstrates an undulating softening behavior. Via a detailed analysis of the simulation results, it was concluded that multiple intermittent occurrences and stops of SIBM on a local scale at different locations within the microstructure result in such an undulating softening behavior of the stress response. A similar reasoning for the experimental irregularities of dynamic SIBM in tantalum has also been proposed by Pedrazas et al. (2014).

Trend 6: The overall rate of SIBM decreases during its propagation due to the increasing number of impeded grain boundary segments, as shown in Fig. 8f. Therefore, the decreasing rate of the macroscale dislocation density and

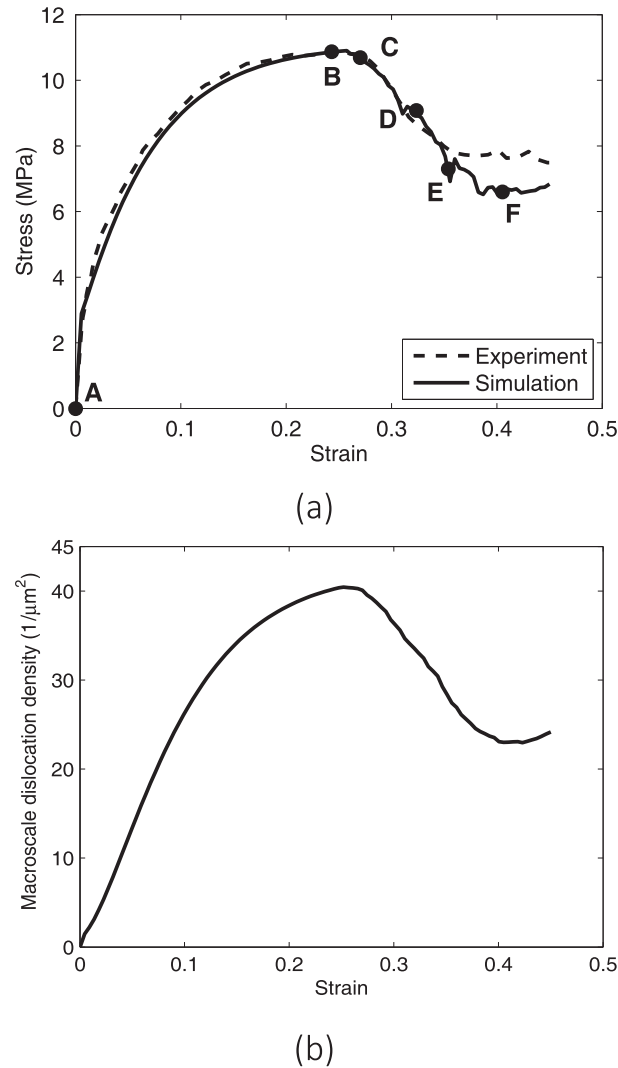


Fig. 7. (a) Numerically simulated stress-strain response of the tantalum polycrystal under uniaxial tensile loading with a constant strain rate and its comparison against the experimental response (Pedrazas et al., 2014). The points labeled as A, B, C, D, E and F are respectively corresponding to the strain values 0.00, 0.24, 0.26, 0.32, 0.35 and 0.40. (b) The evolution of the macroscale dislocation density in the polycrystal as a function of the applied macroscale strain.

consequently the decreasing rate of the macroscopic flow stress reduces while increasing the applied strain, as shown in Fig. 7. Eventually, at some point the hardening rate exceeds the softening rate due to SIBM and hence the macroscopic flow stress stops decreasing. This turning point is identified by point F in Fig. 7a and the corresponding contour plot for the distribution of the mesoscale dislocation density is shown in Fig. 8f. Further increase of the applied strain under constant strain rate beyond this turning point smoothly increases the flow stress again as shown in Fig. 7.

Trend 7: The initial undeformed microstructure shown in Fig. 8a which is composed of equiaxed grains has a log-normal grain size distribution as shown in Fig. 9a. During SIBM, a few grains which are favored by the plastic driving force i.e. the driving force due to the heterogeneity in defect/plastic free energy, consume other grains and abnormally grow in size. Such abnormal grains appear as non-equiaxed large grains in the final microstructure shown in Fig. 8f. As illustrated by the final GSD shown in Fig. 9b, the abnormal grains change the initial log-normal GSD via emerging at larger grain sizes. Comparing the initial and final GSDs in Fig. 9, the initial log-normal GSD appears almost unchanged in shape but reduced in height in the final GSD. The height of the GSD reduces due to the consuming of the equiaxed grains by a few abnormal grains. As identified by arrows in Fig. 9, these abnormal grains appear in the final GSD as low-height single bars at larger grain sizes far away from the log-normal part.

Finally, it is worth mentioning that recent experimental studies on SIBM (Ciulik and Taleff, 2009; Taleff and Pedrazas, 2013; Pedrazas et al., 2014) have partially alluded to the trends described above.

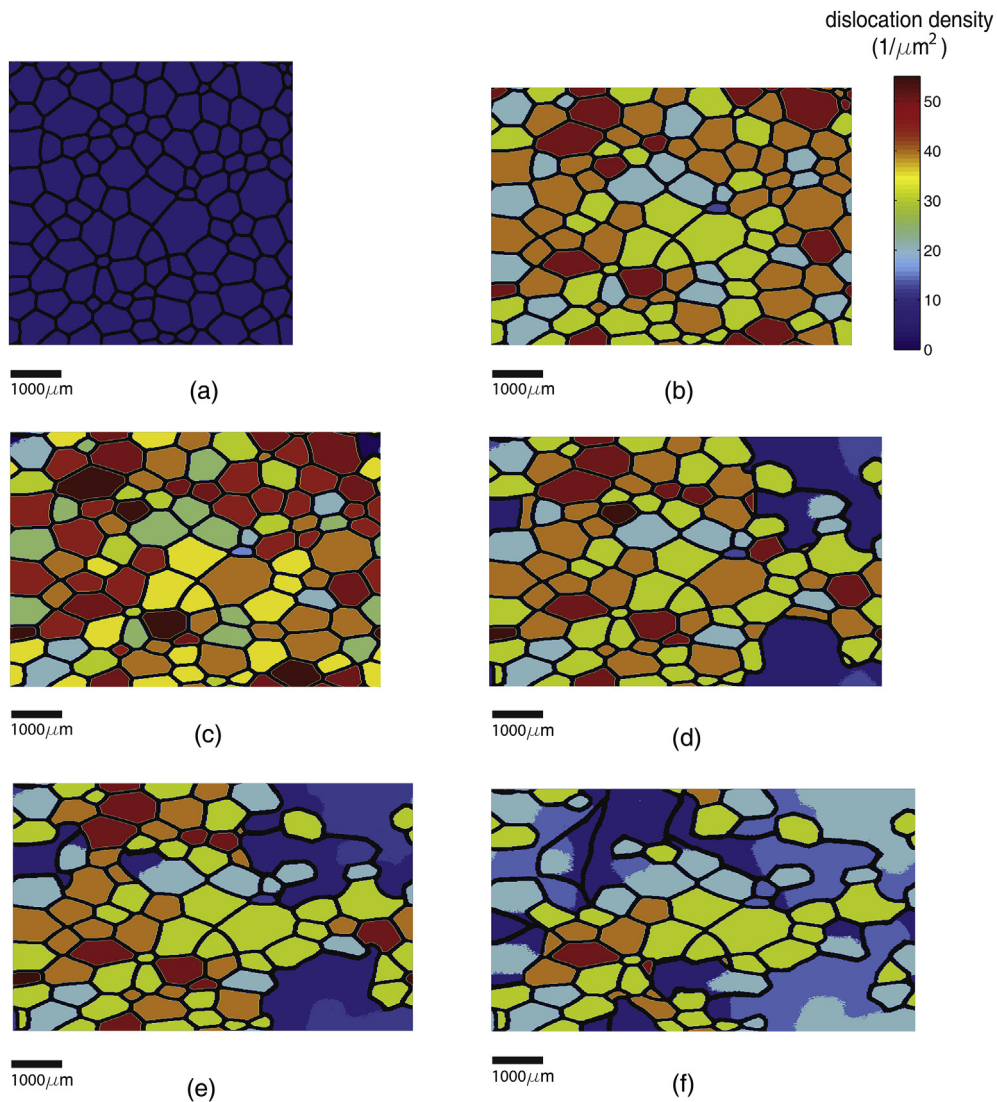


Fig. 8. The contour plots of dislocation density in the tantalum polycrystalline microstructure at different strain values labeled by points (a) A, (b) B, (c) C, (d) D, (e) E and (f) F in Fig. 7a.

6. Conclusions

In this study, the dislocation density-based crystal plasticity and phase field methods were coupled to develop a thermodynamically-consistent finite-deformation-based constitutive theory for describing strain induced grain boundary migration in a plastically deformed polycrystalline RVE. A mesoscale finite-deformation-based constitutive theory was developed using the principle laws of thermodynamics and the theory of microforce balance. By taking the Helmholtz free energy to be a function of dislocation density, the driving forces due to the heterogeneity of the stored deformation energy were included. A Taylor model-based homogenization approach was employed to develop a multiscale sequentially-coupled staggered time integration procedure based on the coupling between finite-element and phase field methods. The numerical algorithm was implemented into the Abaqus/Standard finite element package via writing a user material subroutine UMAT.

The developed constitutive model was then used to perform SIBM simulations in bicrystalline and polycrystalline tantalum. Our numerical simulations qualitatively and also quantitatively match the experimental results of Pedrazas et al. (2014) for SIBM in polycrystalline tantalum. Particularly, the following trends were observed in SIBM simulations.

A minimum critical macroscopic strain value for the initiation of SIBM is observed before which SIBM does not occur because the stored energy difference across the grain boundary has nowhere reached the critical resistance to grain boundary migration. SIBM is initiated by specific grain boundary segments across which the stored energy difference exceeds the critical resistance to grain boundary migration. Initiation of SIBM causes a sudden drop in the macroscopic flow stress. Under

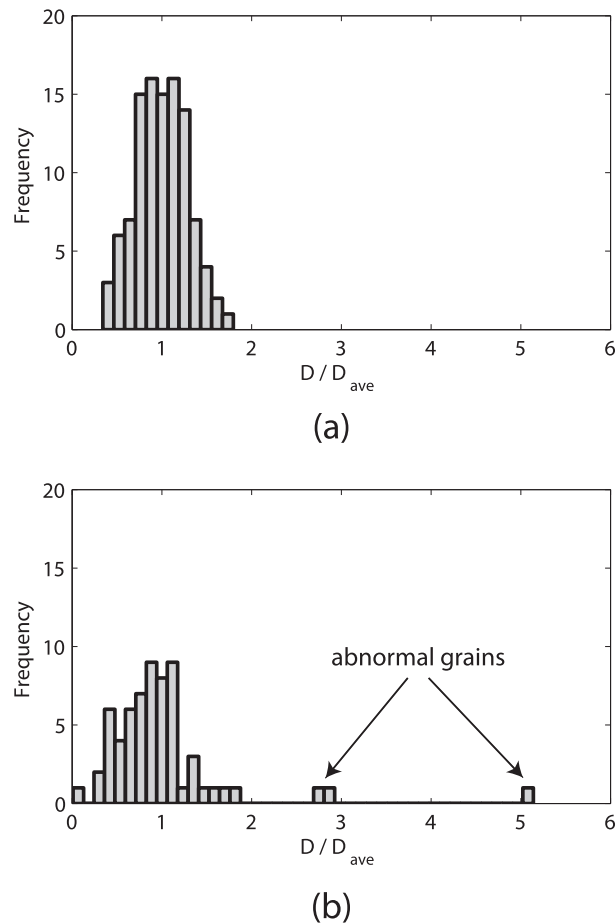


Fig. 9. The grain size distribution histogram for (a) the initial undeformed microstructure labeled by point A in Fig. 7a and (b) the final microstructure labeled by point F in Fig. 7a. The abnormal grains grown by SIBM observed in the microstructure in Fig. 8f are identified by arrows.

constant macroscopic strain rate, the propagation of SIBM causes further reduction of the macroscopic flow stress due to decreasing the dislocation content behind the moving grain boundaries. When the SIBM front encounters a grain with relatively low stored deformation energy, SIBM stops due to the reduction of the driving force below the critical resistance for grain boundary migration. Such obstructing grains are seen as island grains surrounded by the grains grown by SIBM. The overall rate of SIBM decreases during its propagation due to the increasing number of impeded grain boundary segments. Eventually, at some point the hardening rate exceeds the softening rate due to SIBM and hence the macroscopic flow stress stops decreasing.

As a future work, the present model can be augmented by including a description of external surface effects for the modeling of microstructure and texture evolution in polycrystalline thin films. Particularly, the augmented constitutive theory can be developed via supplementing the free energy functional by an additional excess surface free energy term as in the work of Jamshidian et al. (2016).

References

- Abrivard, G., Busso, E., Forest, S., Appolaire, B., 2012a. Phase field modelling of grain boundary motion driven by curvature and stored energy gradients. part i: theory and numerical implementation. *Philos. Mag.* 92, 3618–3642.
- Abrivard, G., Busso, E., Forest, S., Appolaire, B., 2012b. Phase field modelling of grain boundary motion driven by curvature and stored energy gradients. part ii: application to recrystallisation. *Philos. Mag.* 92, 3643–3664. <http://dx.doi.org/10.1080/14786435.2012.717726>.
- Anand, L., 2004. Single-crystal elasto-viscoplasticity: application to texture evolution in polycrystalline metals at large strains. *Comput. Methods Appl. Mech. Eng.* 193, 5359–5383. *Advances in Computational Plasticity*.
- Anand, L., Gurtin, M.E., Reddy, B.D., 2015. The stored energy of cold work, thermal annealing, and other thermodynamic issues in single crystal plasticity at small length scales. *Int. J. Plast.* 64, 1–25.
- Balasubramanian, S., 1998. Doctoral thesis dissertation. Department of Mechanical Engineering, Massachusetts Institute of Technology.
- Battaille, C.C., Counts, W.A., Wellman, G.W., Buchheit, T.E., Holm, E.A., 2007. Simulating grain growth in a deformed polycrystal by coupled finite-element and microstructure evolution modeling. *Metall. Mater. Trans. A* 38, 2513–2522.
- Beck, P.A., Sperry, P.R., 1950. Strain induced grain boundary migration in high purity aluminum. *J. Appl. Phys.* 21, 150–152.

- Bhattacharyya, S., Heo, T., Chang, K., Chen, L., 2011. A phase-field model of stress effect on grain boundary migration. *Modell. Simul. Mater. Sci. Eng.* 19, 035002.
- Bloomfield, M.O., Bentz, D.N., Cale, T.S., 2008. Stress-induced grain boundary migration in polycrystalline copper. *J. Electron Mater.* 37, 249–263.
- Chen, L., Chen, J., Lebensohn, R., Ji, Y., Heo, T., Bhattacharyya, S., Chang, K., Mathaudhu, S., Liu, Z., Chen, L.Q., 2015. An integrated fast fourier transform-based phase-field and crystal plasticity approach to model recrystallization of three dimensional polycrystals. *Comput. Methods Appl. Mech. Eng.* 285, 829–848.
- Chen, L.Q., 2002. Phase-field models for microstructure evolution. *Annu. Rev. Mater. Sci.* 32, 113–140. Cited By (since 1996): 367.
- Ciulik, J., Taleff, E.M., 2009. Dynamic abnormal grain growth: a new method to produce single crystals. *Scr. Mater.* 61, 895–898.
- Franciosi, P., Zaoui, A., 1982. Multislip in f.c.c. crystals a theoretical approach compared with experimental data. *Acta Metall.* 30, 1627–1637.
- Fried, E., Gurtin, M.E., 1994. Dynamic solid-solid transitions with phase characterized by an order parameter. *Phys. D.* 72, 287–308.
- Gurtin, M.E., 2000. On the plasticity of single crystals: free energy, microforces, plastic-strain gradients. *J. Mech. Phys. Solids* 48, 989–1036.
- Gurtin, M.E., 2008. Configurational Forces as Basic Concepts of Continuum Physics, vol. 137. Springer Science & Business Media.
- Gurtin, M.E., Anand, L., Lele, S.P., 2007. Gradient single-crystal plasticity with free energy dependent on dislocation densities. *J. Mech. Phys. Solids* 55, 1853–1878.
- Humphreys, M., Hatherly, F., 2004. *Recrystallization and Related Annealing Phenomena*, second ed. Elsevier.
- Jafari, M., Jamshidian, M., Ziaei-Rad, S., 2017. A finite-deformation dislocation density-based crystal viscoplasticity constitutive model for calculating the stored deformation energy. *Int. J. Mech. Sci.* 128, 486–498.
- Jamshidian, M., Rabczuk, T., 2014. Phase field modelling of stressed grain growth: analytical study and the effect of microstructural length scale. *J. Comput. Phys.* 261, 23.
- Jamshidian, M., Thamburaja, P., Rabczuk, T., 2016. A multiscale coupled finite-element and phase-field framework to modeling stressed grain growth in polycrystalline thin films. *J. Comput. Phys.* 327, 779–798.
- Jamshidian, M., Zi, G., Rabczuk, T., 2014. Phase field modeling of ideal grain growth in a distorted microstructure. *Comput. Mater. Sci.* 95, 663–671.
- Kashihara, K., Konishi, H., Shibayanagi, T., 2011. Strain-induced grain boundary migration in 112;111₁/100;001₂ and 123;634₁/100;001₂ aluminum bicrystals. *Mater. Sci. Eng. A* 528, 8443–8450.
- Kim, S.G., Kim, D.I., Kim, W.T., Park, Y.B., 2006. Computer simulations of two-dimensional and three-dimensional ideal grain growth. *Phys. Rev. E Stat. Nonlinear Soft Matter Phys.* 74.
- Kothari, M., Anand, L., 1998. Elasto-viscoplastic constitutive equations for polycrystalline metals: application to tantalum. *J. Mech. Phys. Solids* 46, 51–83.
- Lee, M., Lim, H., Adams, B., Hirth, J., Wagoner, R., 2010. A dislocation density-based single crystal constitutive equation. *Int. J. Plast.* 26, 925–938.
- Lele, S.P., Anand, L., 2009. A large-deformation strain-gradient theory for isotropic viscoplastic materials. *Int. J. Plast.* 25, 420–453.
- Lim, H., Battaile, C.C., Carroll, J.D., Boyce, B.L., Weinberger, C.R., 2015. A physically based model of temperature and strain rate dependent yield in (BCC) metals: implementation into crystal plasticity. *J. Mech. Phys. Solids* 74, 80–96.
- Moelans, N., 2011. A quantitative and thermodynamically consistent phase-field interpolation function for multi-phase systems. *Acta Mater.* 59, 1077–1086.
- Moelans, N., Blanpain, B., Wollants, P., 2008. Quantitative analysis of grain boundary properties in a generalized phase field model for grain growth in anisotropic systems. *Phys. Rev. B* 78, 025502.
- Noell, J., Taleff, M., 2015. Dynamic abnormal grain growth in refractory metals. *The Journal of the Minerals. Metals Mater. Soc.* 67, 2642–2645.
- Pedrazas, N.A., Buchheit, T.E., Holm, E.A., Taleff, E.M., 2014. Dynamic abnormal grain growth in tantalum. *Mater. Sci. Eng. A* 610, 76–84.
- Popova, E., Staraselski, Y., Brahme, A., Mishra, R., Inal, K., 2015. Coupled crystal plasticity probabilistic cellular automata approach to model dynamic recrystallization in magnesium alloys. *Int. J. Plast.* 66, 85–102. Plasticity of Textured Polycrystals In Honor of Prof. Paul Van Houtte.
- Raabe, D., 2014. 23-recovery and recrystallization: phenomena, physics, models, simulation. In: Laughlin, D.E., Hono, K. (Eds.), *Physical Metallurgy*, fifth ed. Elsevier, Oxford, pp. 2291–2397.
- Raabe, D., Becker, R.C., 2000. Coupling of a crystal plasticity finite-element model with a probabilistic cellular automaton for simulating primary static recrystallization in aluminum. *Modell. Simul. Mater. Sci. Eng.* 8, 445–462.
- Raabe, D., Schlenkert, G., Weissaupt, H., Lücke, K., 1994. Texture and microstructure of rolled and annealed tantalum. *Mater. Sci. Technol.* 10, 299–305.
- de Rancourt, V., Ammar, K., Appolaire, B., Forest, S., 2016. Homogenization of viscoplastic constitutive laws within a phase field approach. *J. Mech. Phys. Solids* 88, 291–319.
- Roters, F., Eisenlohr, P., Hantcherli, L., Tjahjanto, D., Bieler, T., Raabe, D., 2010. Overview of constitutive laws, kinematics, homogenization and multiscale methods in crystal plasticity finite-element modeling: theory, experiments, applications. *Acta Mater.* 58, 1152–1211.
- Sakai, T., Belyakov, A., Kaibyshev, R., Miura, H., Jonas, J.J., 2014. Dynamic and post-dynamic recrystallization under hot, cold and severe plastic deformation conditions. *Prog. Mater. Sci.* 60, 130–207.
- Shanthraj, P., Eisenlohr, P., Diehl, M., Roters, F., 2015. Numerically robust spectral methods for crystal plasticity simulations of heterogeneous materials. *Int. J. Plast.* 66, 31–45. Plasticity of Textured Polycrystals In Honor of Prof. Paul Van Houtte.
- Simmons, G., Wang, H., 1971. *Single Crystal Elastic Constants and Calculated Aggregate Properties. A Handbook*. The MIT Press.
- Steinbach, I., 2009. Phase-field models in materials science. *Modell. Simul. Mater. Sci. Eng.* 17.
- Steinbach, I., Pezzolla, F., 1999. A generalized field method for multiphase transformations using interface fields. *Phys. D.* 134, 385–393.
- Stojakovic, D., Doherty, R., Kalidindi, S., Landgraf, Fernando, J.G.v. p., 2008. Thermomechanical processing for recovery of desired {001} fiber texture in electric motor steels. *Metall. Mater. Trans. A* 39.
- Takaki, T., Yoshimoto, C., Yamanaka, A., Tomita, Y., 2014. Multiscale modeling of hot-working with dynamic recrystallization by coupling microstructure evolution and macroscopic mechanical behavior. *Int. J. Plast.* 52, 105–116. In Honor of Hussein Zbib.
- Taleff, E.M., Pedrazas, N.A., 2013. A new route for growing large grains in metals. *Science* 341, 1461–1462. <http://science.sciencemag.org/content/341/6153/1461.full.pdf>.
- Taylor, G.I., 1938. Plastic strain in metals. *J. Inst. Met.* 62, 307–324.
- Thamburaja, P., Jamshidian, M., 2014. A multiscale taylor model-based constitutive theory describing grain growth in polycrystalline cubic metals. *J. Mech. Phys. Solids* 63, 1.
- Theyssier, M., Driver, J., 1999. Recrystallization nucleation mechanism along boundaries in hot deformed al bicrystals. *Mater. Sci. Eng. A* 272, 73–82.
- Tonks, M., Millett, P., 2011. Phase field simulations of elastic deformation-driven grain growth in 2d copper polycrystals. *Mater. Sci. Eng. A* 528, 4086–4091.
- Tonks, M., Millett, P., Cai, W., Wolf, D., 2010. Analysis of the elastic strain energy driving force for grain boundary migration using phase field simulation. *Scr. Mater.* 63, 1049–1052.
- Vondrou, A., Bienger, P., Schreijöf, S., Selzer, M., Schneider, D., Nestler, B., Helm, D., Mönig, R., 2015. Combined crystal plasticity and phase-field method for recrystallization in a process chain of sheet metal production. *Comput. Mech.* 55, 439–452.
- Yogo, Y., Takeuchi, H., Ishikawa, T., Iwata, N., Nakanishi, K., 2009. Strain-induced boundary migration of carbon steel at high temperatures. *Scr. Mater.* 61, 1001–1003.
- Zhao, L., Chakraborty, P., Tonks, M., Szułfarska, I., 2017. On the plastic driving force of grain boundary migration: a fully coupled phase field and crystal plasticity model. *Comput. Mater. Sci.* 128, 320–330.
- Zhao, P., Low, T.S.E., Wang, Y., Niezgoda, S.R., 2016. An integrated full-field model of concurrent plastic deformation and microstructure evolution: application to 3d simulation of dynamic recrystallization in polycrystalline copper. *Int. J. Plast.* 80, 38–55.